International Journal of Advance Industrial Engineering
E-ISSN 2320 –5539

Available at http://inpressco.com/category/ijaie/

Research Article

Engineered Metal Oxide Nanocomposites and Rare-Earth Doping Strategies for Advanced Photocatalytic Environmental Remediation

[1]Muhammad Nabeel Riaz, [2]Maria Zaib, [2]Muhammad Ali, [2]Fazeela Abdul Sattar, [2]Atiya Fatima, [2]Noor Fatima, [3]Muhammad Amjad, [4]Tehreem Fatima, [5]Alia Ajmal and [*6]Summra Naeem

[1]Department of Environmental Engineering, University of Agriculture Faisalabad, Pakistan
[2]Institute of Natural Sciences, Government College University Faisalabad, Pakistan
[3]Department of Mechanical Engineering, GIKI University of Engineering Sciences and Technology, Pakistan
[4]Department of Chemistry, National University of Sciences and Technology, Pakistan
[5]Department of Chemistry, Kohat University of Science and Technology, Pakistan
[6]Department of Environmental Sciences, University of Engineering and Technology Lahore, Pakistan

Received 20 Aug 2023, Accepted 15 Sept 2023, Available online 22 Sept 2023, **Vol.11, No.3 (Sept 2023)**

Abstract

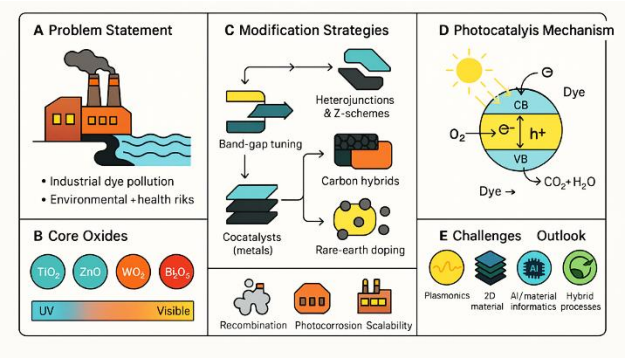

Water pollution from industrial effluents poses a critical global challenge, with synthetic dyes ranking among the most persistent and hazardous contaminants. Their high chemical stability, toxicity, and resistance to biodegradation necessitate advanced treatment methods beyond conventional physicochemical processes. Semiconductor photocatalysis has emerged as a sustainable strategy, exploiting light energy to generate reactive oxygen species that mineralize pollutants into benign products. Classical photocatalysts such as TiO_2, ZnO, WO_3,and Fe_2O_3 exhibit favorable physicochemical properties but suffer from rapid charge-carrier recombination, limited spectral response, and photocorrosion. Recent advances in material engineering, including band-gap tuning, heterojunction construction, catalyst deposition, and carbon-based hybridization, have addressed these limitations. Additionally, rare-earth doping and nanocomposite architectures have demonstrated the ability to extend visible-light activity, enhance structural stability, and improve photocatalytic efficiency. This review synthesizes recent progress in photocatalytic materials and fabrication techniques, with particular emphasis on dye degradation and wastewater remediation. Challenges related to scalability, energy efficiency, and environmental safety are critically examined, and future perspectives are outlined to guide the development of robust, cost-effective, and eco-friendly photocatalytic systems for sustainable water treatment applications.

Keywords: *Water pollution, Synthetic dyes, Semiconductor photocatalysis, Photocatalytic materials, Wastewater remediation*

1. Introduction

Rapid industrialization and population growth have intensified the global freshwater crisis, highlighting the urgent need for advanced wastewater management. Untreated industrial effluents rich in inorganic ions, heavy metals, organics, and persistent contaminants threaten both ecosystems and human health [1, 2]. Synthetic dyes, with complex aromatic structures, resist biodegradation and remain highly toxic. Even in trace amounts, they disrupt photosynthesis, reduce light penetration, and introduce carcinogenic or mutagenic risks to aquatic environments [3].

In response to these challenges, advanced oxidation processes (AOPs) have emerged as powerful alternatives to conventional treatment methods. Semiconductor photocatalysis, in particular, has garnered significant attention as a sustainable technology capable of harnessing solar energy to generate highly reactive oxygen species (ROS), such as hydroxyl radicals (•OH) and superoxide anions ($\bullet O_2^-$), which can mineralize persistent organic pollutants into benign compounds like CO_2 and H_2O [4, 5]. Classic metal oxide semiconductors, including TiO_2, ZnO, WO_3, and Fe_2O_3, have been extensively studied due to their favorable properties, such as chemical stability, non-

*Corresponding author's ORCID ID: 0009-0003-9453-8740
DOI: https://doi.org/10.14741/ijaie/v.11.3.1.1

toxicity, and wide availability [6]. However, their practical application is fundamentally limited by inherent drawbacks, including wide bandgaps restricting absorption to the ultraviolet (UV) spectrum, rapid recombination of photogenerated electron-hole pairs, and susceptibility to photocorrosion, all of which curtail their efficiency and long-term durability.

To overcome these limitations, recent research has pivoted toward sophisticated material engineering and the design of hybrid architectures. This review details the extensive progress in strategies such as band-gap tuning through elemental doping, the construction of heterojunctions (e.g., Type-II, Z-scheme) to enhance charge separation, and hybridization with carbon-based materials (e.g., graphene, carbon dots) to improve electrical conductivity and surface area. A particularly promising avenue, which forms a core focus of this paper, is the doping of these metal oxides with rare-earth (RE) elements (e.g., La, Ce, Nd, Sm, Gd, Eu) [7]. RE doping introduces intermediate energy levels within the bandgap, effectively narrowing it for visible-light absorption, creating charge-trapping sites to suppress recombination, and generating oxygen vacancies that enhance surface reactivity [8, 9]. Furthermore, the development of nanocomposites and tailored nanostructures (e.g., nanorods, hierarchical spheres, core-shell designs) has proven instrumental in optimizing light harvesting and providing abundant active sites for redox reactions [10]. Rare-earth doping and nanocomposite architectures are particularly promising, as they extend light absorption into the visible range, introduce beneficial defect states, and enhance surface reactivity [11]. While these innovations significantly improve degradation efficiency, they also raise critical questions regarding sustainability, cost, and environmental safety when scaled for practical wastewater treatment systems

This review synthesizes the recent advances in engineered metal oxide photocatalysts, with a dedicated focus on ZnO, WO_3, Fe_2O_3, and Bi_2O_3-based systems, for the remediation of dye-laden wastewater. It critically examines the fundamental mechanisms of photocatalysis, the impact of synthesis methods on material properties, and the profound enhancement in performance achieved through rare-earth incorporation and composite formation. While these innovations mark significant progress, the path to large-scale implementation is fraught with challenges. This review therefore also critically addresses the persistent hurdles of catalyst recovery and reusability, the potential environmental implications of nanomaterial release, and the energy efficiency of these processes under real sunlight conditions. By presenting a balanced perspective on both the remarkable capabilities and existing limitations, this discussion aims to guide the rational design of next-generation photocatalytic systems that are not only highly efficient and stable but also cost-effective and environmentally sustainable for real-world water treatment applications.

2. Photocatalysis for Water Treatment

Water contamination remains one of the most pressing global challenges, with pollutants ranging from synthetic dyes and pharmaceuticals to pesticides and heavy metals. Because many of these compounds are chemically stable and resistant to conventional treatment methods, advanced oxidation processes such as photocatalysis have emerged as promising alternatives. Metal-oxide photocatalysts, especially when modified with rare-earth elements or combined into heterostructures, offer efficient pathways for degrading these diverse contaminants under solar or artificial light [12]. As illustrated in Fig. 1, wastewater can be broadly categorized into three primary sources: domestic, industrial, and agricultural effluents. According to a 2016 World Health Organization (WHO) report, over 13.7 million global deaths were linked to exposure to adverse environmental conditions, including workplace and household pollution. Of these, approximately 5.9 million deaths were attributed to air pollution, while poor wastewater treatment was also recognized as a major determinant of ecological and public health outcomes [13]. Each category introduces a diverse set of impurities, contributing to the overall degradation of aquatic environments.

In this context, wastewater treatment has long served as a benchmark application, particularly through studies of dye degradation, where reaction rates and removal efficiencies provide clear insights into photocatalyst performance. Beyond dyes, recent advances demonstrate the capacity of ZnO-based and RE-modified systems to break down pharmaceuticals such as antibiotics, mitigate the toxicity of pesticides, and reduce heavy-metal ions into less harmful forms. These findings highlight water treatment not only as an immediate environmental application but also as a platform for testing design principles that can be extended to energy-related photocatalysis [14].

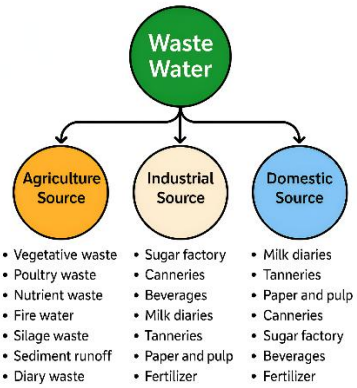

Fig. 1. Sources of wastewater

Given the wide range of pollutants and their varied states, dissolved, dispersed, mobile, or fixed, wastewater treatment requires integrated approaches. Physical, biological, and chemical methods have all been developed, yet their effectiveness depends

heavily on pollutant type, concentration, and treatment infrastructure. Industrial effluents, especially from dye-intensive sectors, remain particularly challenging due to their high toxicity, stability, and resistance to conventional degradation processes.

3. Dyes and Their Impact on the Environment

Water pollution remains a critical environmental and public health challenge, driven by diverse pollutants including pesticides, heavy metals, and synthetic dyes. Among these, dyes are especially problematic due to their stable aromatic ring structures, which render them resistant to biodegradation, heat, light, and oxidizing agents. Even trace concentrations can significantly disrupt aquatic ecosystems, reduce light penetration, impair photosynthesis, and pose carcinogenic or mutagenic risks [15]. For these reasons, dyes are widely regarded as one of the most hazardous classes of pollutants.

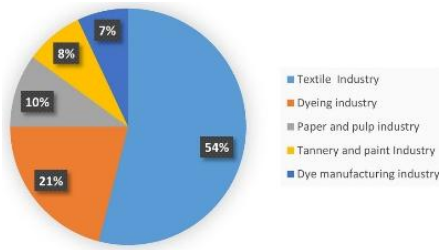

Fig. 2. Dye effluent discharge into the environment [16].

Synthetic dyes are broadly categorized based on their chemical structures and applications. Major classes include azo, anthraquinone, sulfur, indigo, and phthalocyanine dyes, as well as subclasses such as basic, vat, reactive, and dispersion dyes. Each color is associated with a specific molecular structure, and in textile applications dispersion dyes are particularly prominent [17]. Industrial-scale dye production and usage exacerbate the problem: the textile industry alone consumes over 10,000 tons of dyes annually, with an estimated 100 tons discharged daily into wastewater streams [17]. Consequently, textile manufacturing has been identified as one of the most polluting industrial sectors globally, with dye effluents representing a leading contributor to aquatic contamination and ecological degradation [18].

At the molecular level, dye pigments absorb light in the visible spectrum (380–700 nm). The interaction of white light with these pigments, through reflection, diffusion, or transmission, produces the perception of color, a property linked to specific atomic groupings that absorb energy within defined wavelength ranges. While synthetic dyes dominate modern industries, historically most dyes were derived from natural sources such as plants, minerals, and animals. Natural dyes, though less stable, are generally considered safer and less allergenic, and they remain an important area of interest due to their biodegradability [19]. The environmental and health impacts of dyes, as well as their structural diversity and persistence, highlight the urgent need for advanced treatment methods. Figures 2a and 2b illustrate the widespread use of hazardous chemicals in dye production and their uncontrolled release into the environment [16]. A comparative overview of dyes, their chemical formulas, nature, and associated safety concerns is summarized in Table 1.

Table 1. Dyes with corresponding chemical formula and nature

Dye	Chemical Formula	Nature	Safety Concern	Ref
MO	$C_{14}H_{14}N_3NaO_3S$	Acidic	Carcinogenicity	[20]
RBB	$C_{22}H_{16}N_2Na_2O_{11}S_3$	Acidic	Carcinogenicity	[21]
Phenol	C_6H_6O	Acidic	Carcinogenicity	[22]
RhB	$C_{28}H_{31}ClN_2O_3$	Basic	Skin irritation	[23]
MB	$C_{16}H_{18}ClN_3S$	Basic	Eye irritation	[24]
RB	$C_{20}H_4Cl_4I_4O_5$	Acidic	Carcinogenicity	[25]
MR	$C_{15}H_{15}N_3O_2$	Weak acidic	Carcinogenicity	[26]
AV	$C_{20}H_{16}N_4Na_2O_9S_2$	Acidic	Abnormality	[27]
BR	$Cl_9H_{10}Cl_2N_6Na_6O_7S_2$	-	Affects humans	[28]
CR	$C_{32}H_{22}N_6Na_2O_6S_2$	Acid-base	Carcinogenicity	[29]
DB	$C_{34}H_{24}N_6Na_4O_{16}S_4$	-	Mutation	[30]

4. Fundamentals and Mechanism of Photocatalysis

Photocatalysis is fundamentally the acceleration of a photoreaction in the presence of a catalyst. When a semiconductor photocatalyst is irradiated with light of sufficient energy, electron–hole (e^-–h^+) pairs are generated. The photogenerated holes (h^+) oxidize pollutants, while electrons (e^-) reduce species such as O_2, leading to the formation of reactive oxygen species (ROS) including hydroxyl radicals (•OH). These species degrade toxic organic compounds into benign products such as CO_2 and H_2O. The benign nature of the by-products makes photocatalysis a promising technique for industrial effluent treatment.

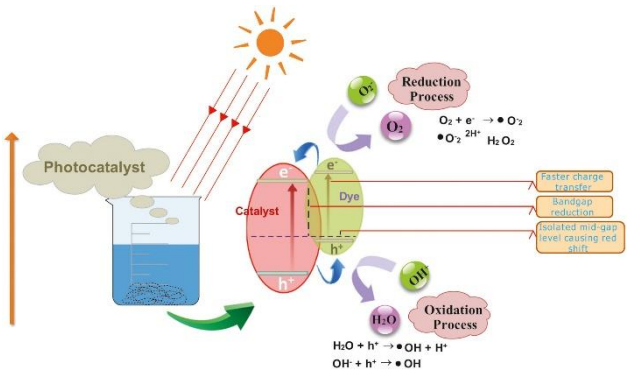

Fig. 3. Photocatalytic mechanism via redox reactions [31].

The basic mechanism is illustrated in Fig. 3. Upon photoirradiation, an electron is excited from the valence band (VB) to the conduction band (CB),

creating a hole in the VB. The resulting e^-–h^+ pair (exciton) initiates redox reactions once adsorbed species interact with the photocatalyst surface. While band structure is critical for most semiconductors, photocatalytic activity can also arise in systems where only localized sites are active [32-34]. Reactants are transferred to the photocatalyst's surface by a multistep process that can be categorized as:1. Electronic reactions involving (a) Adsorption of reactants, (b) Photon's absorption on the surface of catalysts, (c) Exciton formation, (d) Transfer of exciton to reaction sites of photocatalyst's surface. 2. Surface chemical reactions including (a) Reaction among adsorbed species (i.e. both reactants and products).

5. General Mechanism: Reaction Pathway

The primary role of a photocatalyst is to accelerate oxidation–reduction processes under incident visible light. The generally accepted photocatalytic process proceeds in three sequential stages: (i) photoinduced charge-carrier generation (e^-–h^+ pairs); (ii) migration of these charge carriers to the photocatalyst surface; and (iii) surface redox reactions leading to pollutant degradation (Fig. 4) [10].

Upon illumination, electrons (e^-) are excited from the valence band (VB) to the conduction band (CB), leaving behind holes (h^+). These photogenerated charge carriers migrate to the catalyst surface and participate in redox processes. Electrons reduce dissolved oxygen molecules to superoxide radicals (O_2•$^-$), while holes oxidize water molecules to produce hydroxyl radicals (•OH). Both ROS possess strong oxidative and reductive potentials, which drive the degradation of dye molecules into simpler, benign products.

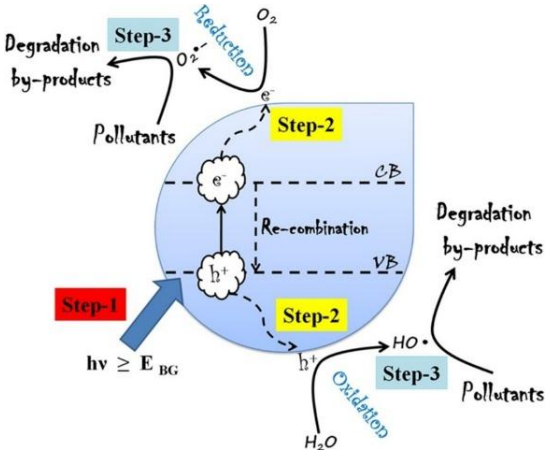

Fig. 4. Schematic of photo-induced e^-/h^+ pairs on photocatalyst surface [35].

Through these interconnected pathways, highly reactive oxygen species generated at the catalyst surface ensure the oxidative mineralization of dye pollutants into non-toxic end products. The schematic mechanism is illustrated in Fig. 4 [35].

6. Surface Chemistry of Photocatalysts

Surface chemistry plays a critical role in photocatalysis, as the nature of interactions between the catalyst surface and surrounding molecules governs charge transfer, ROS formation, and pollutant degradation efficiency. These interactions typically occur with water molecules, organic reactants, and photogenerated intermediates.

6. 1 Interactions with water

Photocatalytic reactions in aqueous systems are strongly influenced by water–surface interactions, which are essential in H_2O splitting, CO_2 reduction, and pollutant degradation. TiO_2, especially rutile, is the most widely studied photocatalyst for water oxidation [36, 37]. Two mechanisms have been proposed: the nucleophilic attack (NA) mechanism, where water attacks oxygen-trapped holes at bridging oxygen sites forming Ti–O•HO–Ti intermediates, and the redox photooxidation (RP) mechanism, where photogenerated holes oxidize adsorbed water to produce OH• radicals [36]. Both share common features such as initiation at bridging oxygen sites, peroxide formation, and proton-mediated electron transfer, particularly at pH < 13.

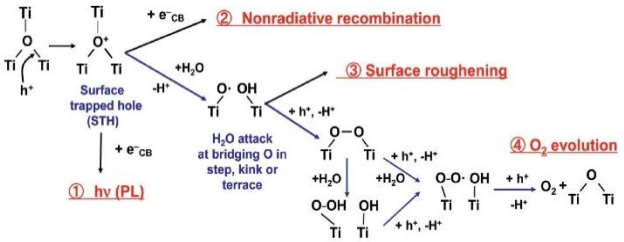

Fig. 5. Water photooxidation and side reactions on rutile TiO_2 surface [36].

Light can also induce hydrophilicity in TiO_2, enhancing water adsorption and contaminant removal. This effect persists even without surface contaminants, indicating intrinsic surface–water interactions. [38, 39]. But surface decomposition is not the only cause and various other factors may also be involved as photoinduced hydrophilicity is observed even in the absence of surface contaminants [40]. Similar processes occur in hematite (α-Fe_2O_3), where Fe=O intermediates are formed during water oxidation. Studies confirmed that hole transfer proceeds via proton-coupled electron transfer, strongly dependent on pH. PEC-IR measurements have identified Fe(IV)=O as a key intermediate [41, 42]. The overall mechanism is summarized in Fig. 5 [36].

6.2 Interactions with reactants

The adsorption of organic molecules also governs photocatalytic activity. Formic acid adsorbs strongly on

TiO_2 and is directly oxidized by valence band holes, while benzene interacts weakly and undergoes indirect oxidation via terminal O• radicals. Phenol competes with water in aqueous systems, leading to indirect oxidation, but in acetonitrile it undergoes direct oxidation at nearly twice the rate [43]. For example, the direct transfer mechanism is followed by formic acid as it is chemisorbed strongly on the surface of TiO_2 in H_2O and directly oxidized by VB holes (Fig. 6a) while an indirect transfer mechanism involving a terminal -Os- radicals are observed for benzene that is physisorbed on TiO_2 surface as chemisorption is not favored for benzene (Fig. 6b). Similarly, Phenol follows either a direct mechanism or indirect mechanism of oxidation depending on the type of solvent. The directindirect mechanism is followed when water is used as solvent where a higher reaction rate is observed for indirect mechanism owing to the competition of H_2O and phenol for binding on TiO_2 surface (Fig. 6c and d). No change in the rate of reaction is observed when water is replaced with acetonitrile in an indirect mechanism while a double increase in the magnitude of reaction rate was observed for the direct mechanism due to negligible interaction of acetonitrile and TiO_2.

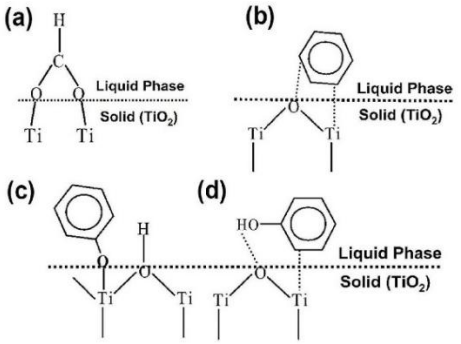

Fig. 6. Interaction modes of reactants on TiO_2: (a) formic acid chemisorption, (b) benzene physisorption, (c) phenol chemisorption, and (d) phenol physisorption. Solid line = covalent bonding; dashed line = weak interactions [44].

Gas-phase CO_2 photoreduction is hindered by weak adsorption, which makes the initial electron transfer unfavorable [45]. Binding at oxygen or cationic sites, or through mixed chemisorption, bends CO_2 and reduces the reduction barrier [46]. Computational studies on Zn_2GeO_4 revealed multiple adsorption modes across crystallographic planes [47, 48]. Improvements in CO_2 reduction have also been achieved through defect engineering and doping; oxygen vacancies and Cu sites in perovskites and MOFs enhance CO_2 adsorption and electron transfer [49-51]. A comparative overview is shown in Fig. 6 [44].

6.3 Interactions with photogenerated species

Surface interactions with intermediates affect both efficiency and stability. On TiO_2, methanol (CD_3OH) dissociates sequentially, forming CD_2O. The rapid desorption of this product enhances turnover, while strong binding slows the process [52]. Other photocatalysts suffer from intermediate accumulation. For example, WO_3 shows reduced stability in $HClO_4$ due to blocking of surface sites by ClO_4• [53] , while g-C_3N_4 undergoes self-poisoning during H_2 evolution as H_2O_2 accumulates, though cocatalysts can decompose H_2O_2 and restore activity [54].

These cases illustrate the trade-off between strong and weak adsorption: strong binding can promote oxidation but also favors recombination and photocorrosion, while weak binding limits charge transfer. To address these challenges, integrated systems combining cocatalysts, light absorbers, and passivation layers have been developed. These architectures mimic natural photosynthesis by enhancing charge separation, extending spectral absorption, and improving durability, as illustrated in Fig. 7 [45].

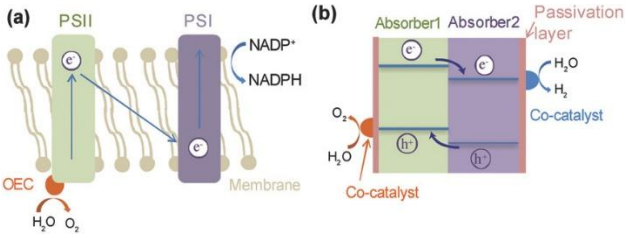

Fig. 7. (a) Artificial photocatalyst system; (b) modified light absorber with co-catalyst and passivation layer [45].

7. Types of Photocatalysis

Photocatalytic reactions are broadly classified as homogeneous or heterogeneous processes. Efficient systems require high surface area, suitable morphology, and an appropriate band gap, along with stability and reusability under reaction conditions [55].

7.1 Homogeneous photocatalysis

In homogeneous photocatalysis, catalysts and reactants exist in the same phase. The most studied examples are the photo-Fenton and ozonation systems. In the photo-Fenton process, light induces the following reactions:

$$H_2O_2 + h\nu \rightarrow 2{\bullet}OH$$
$$Fe^{3+} + H_2O + h\nu \rightarrow Fe^{2+} + {\bullet}OH + H^+$$

These reactions generate highly reactive hydroxyl radicals. The main advantage of this method is the use of visible sunlight (~450 nm), avoiding artificial UV sources. However, it requires acidic conditions and careful removal of Fe ions to prevent secondary pollution. Despite these challenges, •OH radicals produced by such systems are versatile oxidants for pollutant degradation.

7.2 Heterogeneous photocatalysis

Heterogeneous photocatalysis, pioneered by Fujishima and Honda in 1972 with TiO_2 for water splitting, involves catalysts and reactants in different phases. This approach underpins diverse applications, including oxidation, isotope exchange, detoxification of pollutants, and dehydrogenation [56]. Its appeal lies in interdisciplinary foundations, catalysis, photochemistry, spectroscopy, and surface science.

The process initiates with photon absorption by a semiconductor, producing electron–hole pairs:

$$MO + h\nu \rightarrow MO (h^+ + e^-)$$

Holes react with surface water to yield hydroxyl radicals, while electrons reduce oxygen to superoxide:
Oxidation:

$$h^+ + H_2O \rightarrow \bullet OH + H^+$$
$$2h^+ + 2H_2O \rightarrow 2H^+ + H_2O_2 \rightarrow 2\bullet OH$$

Reduction:

$$e^- + O_2 \rightarrow \bullet O_2^-$$
$$\bullet O_2^- + H_2O + H^+ \rightarrow H_2O_2 + O_2 \rightarrow 2\bullet OH$$

These radicals possess strong redox potentials that drive the mineralization of organic contaminants into CO_2 and H_2O [57]. Heterogeneous photocatalysis has thus become a cornerstone for energy production, environmental remediation, and chemical synthesis.

8. Metal Oxide Based Heterostructures for Photocatalytic Applications

8.1 ZnO based photocatalysts

Zinc oxide (ZnO) is an n-type semiconductor characterized by a wide band gap of 3.37 eV and a high exciton binding energy of 60 meV, which enables the generation of electron–hole pairs under ultraviolet and visible light irradiation. Owing to its abundance, low cost, and benign environmental profile, ZnO has become one of the most widely studied photocatalysts for the degradation of organic pollutants. Chen et al. synthesized ZnO nanoparticles (NPs) through a sol–gel route using zinc acetate as the precursor, with calcination at 300–600 °C to obtain crystalline products [58]. By varying the molar ratio of oxalic acid to zinc acetate from 2 to 5, they showed that photocatalytic activity against azo dyes (MO, CR, DB38) improved with higher catalyst dosage, lower initial dye concentration, and acidic conditions, suggesting ZnO's potential as an efficient and sustainable photocatalyst for dye-contaminated wastewater. Gu et al. developed Pt-dispersed ZnO nanorods on carbon fibres (Pt@ZnO) via atomic layer deposition, hydrothermal growth, and magnetron sputtering (Fig. 8) [59].

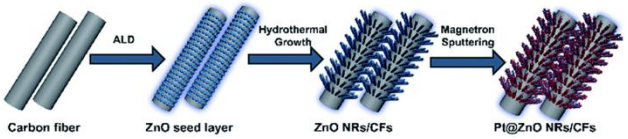

Fig. 8. Schematic diagram of fabrication of Pt@ZnO NRs/CFs composites [59].

Pt nanoparticles (2–5 nm) anchored on ZnO nanorods facilitated efficient charge transfer at the Pt–ZnO interface, suppressing electron–hole recombination. This hierarchical photocatalyst demonstrated superior performance in degrading methyl orange compared with unmodified ZnO nanorods, alongside excellent stability and recyclability, highlighting its practical potential. Nekouei et al. introduced ZnO nanoplatelets modified with activated carbon derived from Konar bark [60]. The ZnO–AC system achieved effective ciprofloxacin (CIP) removal under visible light, with kinetics following a pseudo-first-order model. Degradation intermediates were identified using UPLC-MS/MS, marking the first use of activated carbon-modified ZnO for CIP degradation.

Atchudan et al. synthesized a hybrid ZnO@N-C composite, comprising ZnO nanoparticles embedded in nitrogen-doped graphitic carbon sheets along with nitrogen-doped carbon dots (N-CDs), via a hydrothermal process using peach fruit juice [61]. The hybrid achieved >95% methylene blue (MB) degradation within 60 minutes under UV light. The synergistic interaction between ZnO, N-C, and N-CDs promoted efficient charge transfer and stability, while the bio-derived synthesis underscored its economic and eco-friendly appeal. Notably, the N-CDs also exhibited strong fluorescence with high quantum yield and water solubility, enabling potential use in bioimaging. Hassan et al. reported ZnO nanoparticles synthesized using Coriandrum sativum leaf extract, which acted as a green reducing and stabilizing agent [62]. These particles showed ~96% anthracene degradation at room temperature and neutral pH under UV irradiation for 240 minutes. The reaction kinetics followed a Langmuir–Hinshelwood model, and anthraquinone was identified as the major degradation product by HPLC and GC–MS, confirming the effectiveness of this simple, eco-friendly approach.

Bae et al. fabricated ZnO–Cu_2O hybrid nanoparticles consisting of ZnO cores and Cu_2O nanocube shells, designed as photocatalysts for CO_2 conversion to methane in aqueous media [63]. Operating under ambient conditions, the system achieved a methane production rate of 1080 μmol g_cat^{-1} h^{-1} with >99% selectivity. The exceptional performance was attributed to optimized band alignment, low surface defect density, and a high surface area morphology, which enhanced charge transfer and minimized recombination. Turkyılmaz et al. synthesized ZnO and transition metal-doped ZnO nanostructures via hydrothermal methods and reported band gaps of 3.24 eV (ZnO), 3.15 eV (Ag/ZnO), 3.10 eV (Ni/ZnO), 3.05 eV

(Fe/ZnO), and 3.00 eV (Mn/ZnO) [64]. Photocatalytic testing revealed that Ni/ZnO exhibited the highest efficiency, achieving 98.2% tartrazine degradation within 60 minutes, while Mn/ZnO performed poorest. The proposed mechanism (Fig. 9) suggested that Ni and Ag enhanced charge separation synergistically, whereas Fe and Mn acted antagonistically.

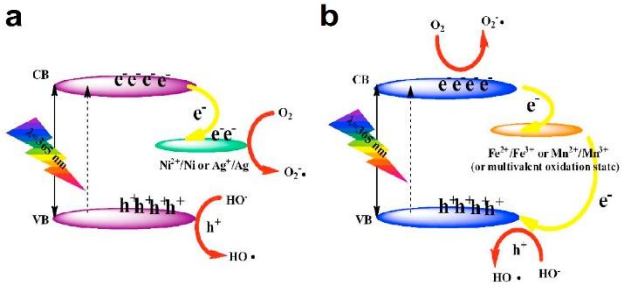

Fig. 9. Mechanisms and charge separation in (a) monovalent and (b) multivalent metal-doped ZnO [64].

ZnO nanoparticles were also successfully anchored onto multi-walled carbon nanotubes (MWCNTs) by a simple chemical method [65]. The ZnO/MWCNT composites showed improved photoelectrochemical water splitting efficiency and significantly enhanced methylene blue degradation compared with pure ZnO. At +1 V vs Ag/AgCl, photocurrent density increased fivefold due to the conductive CNT scaffold, which facilitated charge separation and transport. Electrochemical impedance spectroscopy confirmed faster interfacial charge transfer in the composites. Similarly, one-dimensional heterostructures comprising CuO nanowire cores, In_2S_3 intermediate layers, and ZnO nanorod sheaths ($CuO/In_2S_3/ZnO$) were fabricated through sequential growth steps [66]. These ternary heterostructures exhibited excellent photocatalytic degradation of rhodamine 6G under UV light, surpassing single- and binary-component counterparts, and retained high activity after multiple reuse cycles, demonstrating structural robustness.

Ag_2S-decorated ZnO nanowires (Ag_2S@ZnO) exploited the piezotronic effect to achieve enhanced photocatalysis under simultaneous ultrasonic and solar stimulation [67]. Decorating ZnO with narrow-bandgap Ag_2S extended light absorption into the visible range, while piezocharges generated under strain promoted interfacial charge transfer. The hybrid system retained high activity across eight reuse cycles, outperforming bare ZnO. ZnO nanorod–reduced graphene oxide (rGO) nanocomposites, prepared by electrostatic assembly and hydrothermal reduction, also displayed remarkable activity [68]. ZnO–5% rGO composites degraded rhodamine B six times faster and phenol three times faster than pure ZnO nanorods, with enhanced charge separation and higher surface area attributed to intimate ZnO–rGO coupling.

Computational studies have revealed that ZnO/MoS_2 and $ZnO/MoSe_2$ heterostructures, formed via van der Waals interactions, exhibit narrowed band gaps compared with their individual monolayers, shifting absorption toward visible light [69]. These heterostructures offer promising prospects for photocatalytic water splitting. Experimentally, ZnO/CuO nanofibres synthesized by electrospinning showed superior activity at 0.5 wt% CuO content under sunlight irradiation [70]. Density functional theory (DFT) calculations confirmed that Cu incorporation modulated the band structure and suppressed recombination, consistent with photoluminescence and photocurrent studies. Porous ZnS, ZnO, and ZnS–ZnO nanosheets prepared by thermal annealing demonstrated that ZnS–ZnO heterostructures achieved the highest rhodamine B degradation due to their large surface area and favorable heterointerface [71].

ZnO/ZCIS (CuInZnS quantum dot) composites synthesized at 400 °C demonstrated improved Orange II degradation under simulated sunlight compared with pristine ZnO, attributed to extended visible-light absorption and improved charge transfer at the ZnO–ZCIS junction [72]. Rocksalt-phase ZnO stabilized at ambient conditions by high-pressure torsion reduced the band gap to 1.8 eV, enabling visible-light photocatalysis [73]. Hong et al. reported CuS/ZnO nanowires aligned on stainless steel mesh that showed high piezo-photocatalytic efficiency for pollutant degradation using combined solar and ultrasonic stimulation [74]. The synergy between built-in heterojunction fields and piezoelectric polarization enhanced charge separation and activity.

Hybrid ZnO–carbon systems have also drawn increasing interest. Thangavel et al. synthesized graphdiyne–ZnO nanohybrids with a twofold higher rate constant for azo dye degradation compared with pure ZnO [75]. Au–Ag bimetallic nanoparticle-modified ZnO composites exhibited tunable plasmonic properties that improved photocatalytic RhB degradation and hydrogen production, with performance influenced by the Au/Ag ratio and associated defect states [76]. Ma et al. constructed a CdS quantum dot–ZnO nanosheet heterojunction with a 0D/2D architecture [77]. The intimate CdS–ZnO contact formed a Z-scheme charge transfer pathway, significantly enhancing water-splitting hydrogen evolution efficiency. The system exhibited strong stability, maintaining activity over five cycles within 25 hours.

ZnO-based photocatalysts have also proven effective for solar hydrogen production. Bak et al. synthesized ZnS cores with ZnO shells via partial oxidation [78]. The ZnO shell, enriched with oxygen vacancies, facilitated proton adsorption and improved charge separation, achieving hydrogen evolution rates of 1665 μmol g^{-1} h^{-1} under one-sun irradiation. Photoluminescence confirmed enhanced visible light response after oxidation. Cheng et al. prepared ZnO/γ-Al_2O_3 nanofibres by electrospinning and calcination, which exhibited strong adsorption of methyl orange and Cr(VI) ions [79]. Decoration with Ag nanoparticles further enabled photocatalytic MO degradation under

UV light, combining adsorption and photocatalytic functions with excellent reusability.

Rare-earth doping has been effective in suppressing recombination. Alam et al. synthesized ZnO doped with La, Nd, Sm, and Dy by sol–gel methods, finding Nd–ZnO achieved the best performance with 98% MB degradation and 68% TOC mineralization within 180 minutes [80]. Hollow ZnO microspheres prepared hydrothermally within 30 minutes displayed enhanced barrier properties when incorporated into polyacrylate composites, with increased water resistance and reduced permeability [81]. Mn-doped ZnO synthesized by wet-chemical methods exhibited improved MB degradation under visible light compared with undoped ZnO, due to Mn^{2+} tail states narrowing the band gap [82].

NiO–Fe_2O_3–ZnO ternary layers grown on polyimide films through alkaline modification and ion-exchange formed heterostructures with superior photocatalytic activity compared with binary systems [83]. XRD, XPS, and FTIR confirmed successful heterostructure formation, while SEM revealed uniform nanoparticle dispersion. Under solar irradiation, methyl orange degradation reached 96.2% within 240 minutes, attributed to efficient vectorial charge transfer among ZnO, NiO, and Fe_2O_3. Three-dimensional ZnO flower-like architectures, assembled from ultrathin nanosheets in a solvothermal system, achieved extraordinarily high adsorption capacities for triphenylmethane dyes, with 7154.9 mg/g for acid fuchsin, the highest reported to date [84]. The mechanism was linked to electrostatic interactions and ion-association complexes. Finally, Isimjan et al. constructed a ZnO/Pt/CdZnS Z-scheme catalyst where Pt nanoparticles were positioned between ZnO and CdZnS [85]. The $[ZnO]_4$/1 wt%Pt/CdZnS system achieved a quantum yield of 34% at 360 nm, 2.5 times higher than Pt/CdZnS, with transient absorption spectroscopy confirming the Z-scheme charge transfer. Catalyst stability was largely dependent on sacrificial reagents and pH.

8.2 WO_3 based photocatalysts

Tungsten oxide (WO_3) is an inexpensive semiconductor photocatalyst valued for its stable physicochemical properties, narrow band gap (2.4–2.8 eV), strong response to visible light, high valence-band hole oxidation ability, and low toxicity [86]. Despite these advantages, pure WO_3 suffers from rapid electron–hole recombination and a conduction band potential more positive than the O_2/O_2^- reduction potential, limiting oxygen activation during photocatalysis [87, 88]. These drawbacks hinder its large-scale application. To address them, strategies such as morphology control, noble metal deposition, elemental doping, heterojunction formation, and carbon-based modifications have been widely explored to tune WO_3's structure and band gap, thereby enhancing photocatalytic efficiency [89, 90]. This section reviews recent advances in WO_3-based photocatalysts for wastewater treatment.

Yao et al. synthesized hierarchical WO_3 nanosheets via a surfactant-free hydrothermal route, confirmed by XRD, SEM, and TEM (Fig. 11). The material efficiently degraded methylene blue (MB), eosin red (ER), and congo red (CR) under visible light, demonstrating potential for wastewater purification [91]. Using a similar hydrothermal method, the group later produced WO_3 nanorods that also exhibited superior dye degradation performance, further confirming the suitability of WO_3 nanostructures for environmental remediation [92].

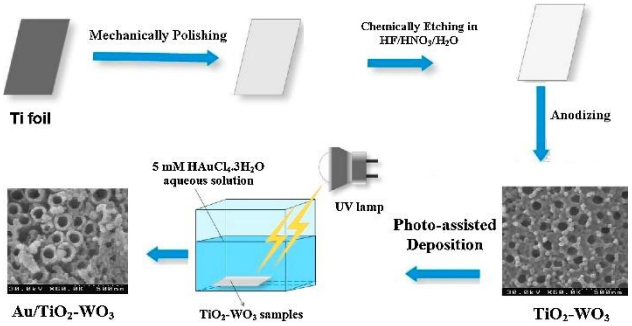

Fig. 10. Preparation of Au/TiO_2–WO_3 composite electrode [93].

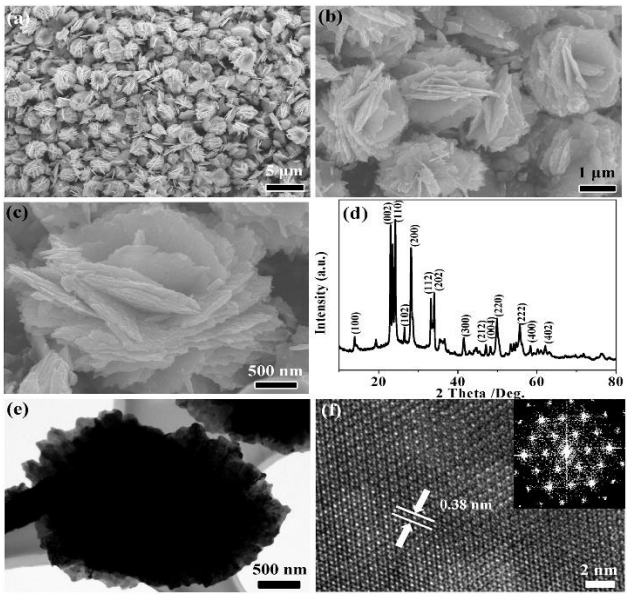

Fig. 11. (a–c) SEM, (d) XRD, and (e, f) TEM of WO_3 hierarchical structures [91].

Wang et al. reported hierarchical double-shell WO_3 microspheres (HDS-WO_3), synthesized from $WO_3 \cdot H_2O$ using $CaCl_2$ templates. These microspheres achieved excellent MB degradation under visible light compared with conventional WO_3 [94]. Yu et al. showed that flower-like hierarchical porous WO_3, prepared hydrothermally, outperformed non-porous analogues for RhB degradation, owing to hierarchical pores that enhanced light and reactant transport [95]. Similarly, Adhikari et al. demonstrated that WO_3 nanorods

exhibited higher RhB degradation efficiency than nanoparticles [96]. Guo et al. compared $WO_{2.72}$ nanowires and urchin-like $WO_{2.72}$ nanostructures prepared solvothermally, finding that one-dimensional nanowires provided superior photocatalytic activity under UV light, while both morphologies outperformed commercial WO_3 [97].

Doping and composite strategies have also enhanced WO_3 photocatalysis. Mehmood et al. prepared Ni-doped WO_3 nanoplates via co-precipitation, achieving improved methyl red degradation due to reduced band gap [98]. Pirzada et al. synthesized Mo-doped WO_3/TiO_2 nanocomposites, which degraded MB and p-chlorophenol more effectively than undoped WO_3/TiO_2, attributed to improved charge separation [99]. Zhang et al. fabricated flower-like WO_3 nanosheets decorated with Ag nanoparticles. The plasmonic effect of Ag enhanced visible light absorption, boosting MB and 2-chlorophenol degradation compared with bare WO_3[100]. Mehmood et al. also investigated Fe-doped WO_3 nanoplates, reporting significantly improved methyl red degradation efficiency relative to undoped WO_3 [101].

Momeni et al. adopted a photo-assisted deposition (PAD) method in order to achieve highly dispersed gold (Au) nanoparticles on TiO2-WO3 nanotubular composite electrodes via one-step electroche mical anodizing. Also, the schematic presentation of the fabrication of Au/TiO2-WO3 composite electrode is displayed in Fig. 10. The photocatalytic activity of the samples was evaluated towards the degradation MB and found that degradation ability of Au/TiO2-WO3 nanotubes was greatly enhanced when compared with that of bare TiO2-WO3 nanotubes. Hence, this work opened a new way to design and synthesis a novel TiO2-WO3 nanotubes materials for environmental remediation work [93]. Noble metal deposition further improves photocatalysis. Momeni et al. employed photo-assisted deposition to anchor Au nanoparticles onto TiO_2–WO_3 nanotube composites (Fig. 10). The Au/TiO_2–WO_3 system showed markedly enhanced MB degradation relative to bare nanotubes, illustrating the role of Au in facilitating charge transfer and reducing recombination [100]. Ma et al. developed WO_3/Cu(II) composite nanofibres that significantly outperformed pure WO_3 for RhB and aniline degradation, with 2% Cu(II) doping yielding the highest activity due to enhanced visible-light absorption [102].

Carbon-based composites have also gained prominence. Ahmed et al. synthesized WO_3 nanosheets and reduced graphene oxide/WO_3 (rGO/WO_3) composites hydrothermally, with the latter outperforming bare WO_3 in MB and RhB degradation under sunlight due to improved charge separation [104]. Zhou et al. fabricated WO_3 nanorod/graphene (WO_3@GE) composites with superior MO degradation compared to bare WO_3 nanorods [105].

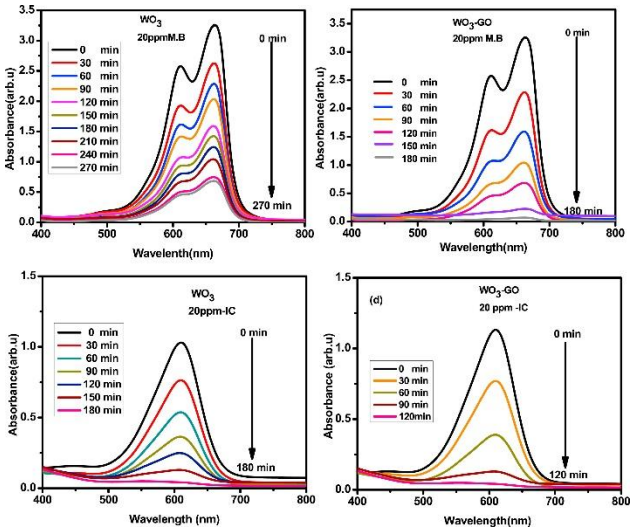

Fig. 12. Absorbance spectra of MB (a, b) and IC (c, d) over WO_3 and WO_3–GO photocatalysts under sunlight [103].

An et al. reported similar WO_3/graphene composites with significant RhB degradation enhancement under visible light [106]. Gan et al. prepared WO_3/graphene composites with varying graphene loadings, identifying WO_3/G-7 (7 wt% graphene) as optimal for MB degradation, due to narrowed band gap and improved conductivity [107].

Other carbon-based designs include Taha et al.'s porous WO_3–carbon nanofibre (WO_3–CNF) composites synthesized by electrospinning. These materials showed outstanding MB, MO, and malachite green degradation efficiencies compared with pure WO_3, confirming CNF's role in improving light absorption and charge separation [108]. Farhadian et al. developed WO_3/MWCNT composites via liquid-phase synthesis. The composites exhibited improved naphthalene degradation under visible light, attributed to high conductivity and reduced recombination [109]. Song et al. reported C-dot/WO_3 composites prepared by hydrothermal methods, achieving excellent RhB degradation due to synergistic light harvesting and charge separation [110]. Ismail et al. synthesized mesoporous WO_3 and WO_3–GO nanocomposites, subsequently incorporating Pt nanoparticles. Pt/WO_3–GO composites displayed photodegradation rates 3, 2, and 1.15 times higher than mesoporous WO_3, WO_3–GO, and Pt/WO_3, respectively, owing to synergistic electron transfer and enhanced O_2 reduction [111]. Jeevitha et al. ultrasonically prepared WO_3–GO nanocomposites, achieving superior MB and indigo carmine degradation under sunlight compared with bare WO_3 (Fig. 12) [103].

8.3 Fe_2O_3 based photocatalysts

Iron oxide (Fe_2O_3) exists in several stoichiometric and crystalline forms, of which α-Fe_2O_3 (hematite) is the most stable. Its structure comprises hexagonally arranged Fe atoms surrounded by six O atoms in a corundum lattice (space group R-3c, lattice parameters

a = 5.0356 nm, c = 13.7489 nm, six formula units per unit cell). Compared with TiO_2, Bi_2O_3, or ZnO, Fe_2O_3 offers a narrower band gap (~2.2 eV), low cost, natural abundance, chemical stability, and nontoxicity, making it suitable for photocatalytic applications such as water treatment and water splitting. However, its practical efficiency is restricted by short hole diffusion lengths (2–4 nm), high electron–hole recombination, and poor conductivity. To overcome these issues, researchers have pursued nanostructuring, doping, conductivity enhancement, and surface modification strategies [112]. Sundaramurthy et al. reported Fe_2O_3-mediated Congo red degradation through charge transfer from dye LUMO levels to the Fe_2O_3 conduction band. Reactive species including O_2•– and HO_2• facilitated dye mineralization into nontoxic products [113]. Reducing Fe_2O_3 to nanocrystalline form by hydrothermal, solvothermal, co-precipitation, combustion, or ionic liquid-assisted synthesis significantly improves photocatalysis due to increased surface area and active sites [114, 115].

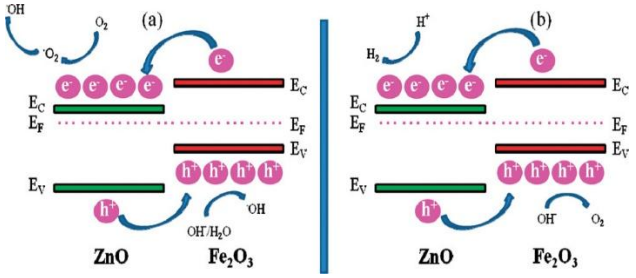

Fig. 13. Photocatalytic (a) dye degradation and (b) H_2 generation [116].

Hydrothermally synthesized α-Fe_2O_3 with uniform 170 nm size demonstrated superior magnetic and photocatalytic properties, while 25–55 nm nanoparticles effectively decomposed H_2S gas [117]. Thermal dehydration yielded α-Fe_2O_3 nanorods with higher RhB degradation efficiency than micron rods, confirming that crystallite downsizing enhances activity [118]. Nanoparticles as small as 5.4 nm achieved oxygen evolution rates of 1072 μmol g^{-1} h^{-1}, far exceeding bulk powders. Calcination temperature, catalyst dosage, pH, and illumination intensity also play vital roles, as shown by Dang et al. and Soni et al., who demonstrated improved activity at higher calcination temperatures, alkaline conditions, and elevated light intensities [119, 120]. Liu et al. optimized catalyst loading at 50 mg/L, while porosity was shown to directly correlate with activity due to enhanced dye–catalyst interaction [121, 122]. Hydrothermal α-Fe_2O_3 nanospheres exhibited activity twice that of nanopowders and 12 times that of micron powders [123].

Morphology strongly influences performance. Flower-like α-Fe_2O_3 structures synthesized by biphasic interfacial reactions outperformed commercial powders in RhB degradation due to higher porosity and surface area. Hollow microspheres facilitated improved charge separation, multiple internal reflections, and better OH radical generation, producing superior dye degradation [124, 125]. Oxygen pressure also enhanced activity by increasing the availability of reactive species such as HO•, O_2•–, and HO_2• [126]. Surface modification and doping further improve photocatalysis. Yeast-templated α-Fe_2O_3 calcined at 300 °C exhibited high surface area and activity, while Al-doped α-Fe_2O_3 benefited from optimized pore size distribution. Noble metals such as Pt and Au enhanced MB degradation through improved charge separation [127]. Mixed oxides such as Fe:Zn and Ce:Fe prepared via combustion showed superior degradation of chloronitrophenol and Rhodamine 6G, with the mechanism depicted in Fig. 13 [116].

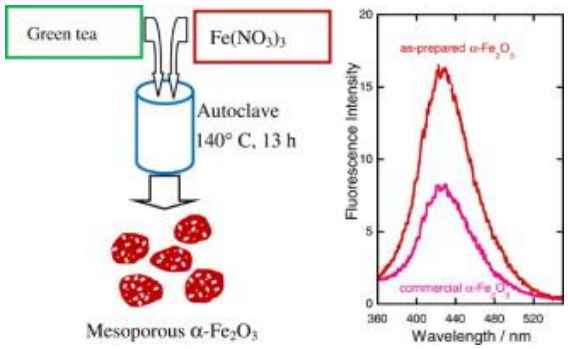

Fig. 14. Green synthesis and photocatalytic activity of α-Fe_2O_3 [128].

Anionic dopants such as F and N created additional acceptor states, enhancing charge separation and reducing recombination, while carbon nanostructures improved electron storage and photocatalytic efficiency. Carbon quantum dot-doped α-Fe_2O_3 degraded benzene and methanol vapors, while GO/α-Fe_2O_3 composites efficiently degraded toluene with good recyclability [126][129].

Thin-film engineering has emerged as a promising route to enhance activity. RF magnetron-sputtered α-Fe_2O_3 thin films exhibited improved photocatalytic performance due to optimized thickness, crystallinity, and surface roughness [130]. Films deposited on $SrTiO_3$ or SnO_2 substrates showed enhanced photocurrent and improved degradation of 2-naphthol. Thermal oxidation yielded α-Fe_2O_3 nanorod films that degraded 99% RhB within 6 h [131].

Green synthesis routes have also been explored. Mesoporous α-Fe_2O_3 nanoparticles (60 nm) prepared using eco-friendly methods displayed twice the hydroxyl radical formation and photocatalytic activity compared with commercial α-Fe_2O_3, as confirmed by fluorescence spectroscopy (Fig. 14) [128]. Dopants such as Ni, Sn, and Ti have further improved conductivity, mobility, and hole generation, enhancing photocurrent density. For instance, Ti-doped α-Fe_2O_3 increased photocurrent from 0.15 to 1.2 mA cm^{-2}, while Ni incorporation enhanced charge transfer [135][132, 133].

In summary, α-Fe_2O_3 has been extensively studied for photocatalytic dye degradation, gas decomposition, and water splitting. Strategies such as nanoscaling, morphology engineering, doping, hybridization with carbon materials, and thin-film fabrication have significantly improved charge separation, conductivity, and visible-light activity. Despite intrinsic limitations, optimized α-Fe_2O_3 nanostructures demonstrate strong potential as cost-effective, stable, and sustainable photocatalysts for environmental remediation.

8.4 Bi_2O_3 based photocatalysts

Bismuth oxide (Bi_2O_3) is a p-type semiconductor with a direct band gap of approximately 2.8 eV. Its relatively narrow band gap, strong optical–electronic response, excellent electrical conductivity, and high photoconductivity make it attractive for photocatalytic applications. Bi_2O_3 is non-toxic, non-carcinogenic, and environmentally benign, which further strengthens its potential for wastewater remediation under visible light irradiation. Importantly, Bi_2O_3 exists in six polymorphs, α (monoclinic), β (tetragonal), γ (cubic bcc), δ (cubic fcc), ε (orthorhombic), and ω (triclinic), providing structural flexibility for tailoring photocatalytic properties [134]. However, bulk Bi_2O_3 alone typically exhibits low photocatalytic efficiency due to rapid recombination of charge carriers. As such, research has focused on engineering nanostructures, controlling polymorphism, doping with metals, and constructing heterojunctions with other semiconductors to enhance photocatalytic activity.

Similarly, flower-like β-Bi_2O_3 micro/nanostructures prepared using L-asparagine-assisted reflux-calcination displayed excellent degradation of 4-phenylphenol under solar light, with optimum performance achieved at 340 °C. The enhanced activity was attributed to high surface area and stable morphology [135]. Microwave-assisted synthesis of α- and β-Bi_2O_3 nanoparticles revealed enhanced photocatalysis by β-Bi_2O_3 toward Rhodamine B (RhB), consistent with its structural advantages [136]. Nanowires of Bi_2O_3 also demonstrated significant visible-light-driven RhB degradation, highlighting the role of one-dimensional morphologies in promoting charge transport. Tubular Bi_2O_3 nanostructures, compared with $(BiO)_2CO_3$ nanosheets, displayed higher RhB degradation rates due to their ability to trap and guide photons within hollow channels, thereby increasing light utilization. Nanocrystalline Bi_2O_3 thin films prepared by chemical bath deposition followed by annealing at 600 °C showed notable activity in RhB degradation under visible light [137]. Furthermore, α-Bi_2O_3 nanorods synthesized hydrothermally degraded methylene blue (MB) efficiently under UV irradiation, again underscoring morphology-driven performance [138].

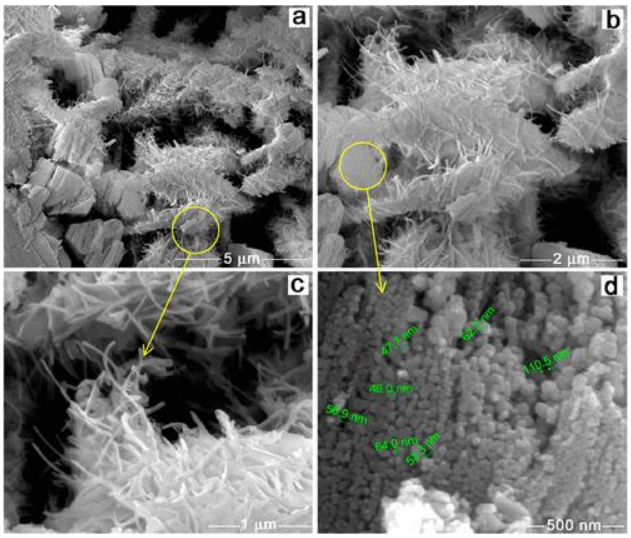

Fig. 15. HR-SEM of Bi_2O_3–ZnO heterostructure [139].

Wu et al. compared plate-like and needle-like Bi_2O_3 prepared by aqueous precipitation and found that plate-like crystals outperformed needle structures in MB degradation, attributed to the exposure of active facets and reduced defect states [140]. Likewise, ultrasound-assisted synthesis of Bi_2O_3 nanoplates improved photocatalysis toward RhB and indigo carmine (IC), while multifunctional porous nanospheres (PNs) synthesized via PVP-assisted hydrothermal routes exhibited enhanced CR and RhB degradation due to their porous framework, which promoted mass transfer and charge migration. Needle-like Bi_2O_3 prepared using ionic liquids effectively degraded malachite green, highlighting versatility in morphology-dependent performance [141].

Three-dimensional architectures, particularly flower-like β-Bi_2O_3 microspheres prepared by hydrothermal methods, also showed outstanding RhB degradation due to their higher surface area and narrower band gap [142]. Similarly, metastable pumpkin-shaped β-Bi_2O_3 demonstrated high photocatalytic efficiency for RhB removal. Fluorine doping into β-Bi_2O_3 rod-like microstructures or α/β phase composites enhanced electron–hole separation and oxidation power of holes, resulting in improved visible-light activity [143, 144]. Hydrothermally synthesized 3D flower-like Bi_2O_3 with controlled α–β phase transitions, induced by acetic acid and calcination temperature, further achieved superior degradation of RhB and sulfamethoxazole (SMX), attributed to mixed phase composition and increased β-phase fraction [145].

Construction of α/β Bi_2O_3 heterojunctions has been widely explored. Bi_2O_3 nanowires containing α/β phase interfaces demonstrated better RhB and MO degradation than single-phase α-Bi_2O_3 due to more efficient charge separation across the junction [146]. Solvothermal-calcination methods yielded α/β Bi_2O_3 photocatalysts that degraded 17α-ethinylestradiol efficiently, while solid-state reactions between α- and β-Bi_2O_3 produced composites with superior

performance in degrading IC and RhB under both UV and visible light [146] [149]. These results consistently indicate that α/β phase heterostructures outperform their pure-phase counterparts due to synergistic electron–hole separation.

Doping has proven to be one of the most effective strategies for tuning the photocatalytic activity of Bi_2O_3. Ag-loaded β-Bi_2O_3 microspheres exhibited higher RB degradation efficiency under visible light than pure β-Bi_2O_3, benefiting from plasmonic effects that facilitated charge carrier migration [147]. Co-precipitation of Ag-doped Bi_2O_3 with varying Ag content revealed that 3 mol% Ag yielded optimal MO degradation. Au-loaded α-Bi_2O_3 microrods significantly enhanced RhB and 2,4-dichlorophenol degradation due to electron trapping at the Au nanoparticles [148].

Other dopants, including Dy, Cu^{2+}, Y^{3+}, Gd^{3+}, Sr^{2+}, Ce, Nd, and Fe, have also been investigated. Dysprosium-doped Bi_2O_3 (3/100 Dy) synthesized via sol-gel method achieved superior MO degradation compared to undoped Bi_2O_3 [149]. Cu^{2+} doping at 5/500 molar ratio enhanced RhB degradation by narrowing the band gap and facilitating charge separation [159]. Y^{3+} and Gd^{3+} doping at optimal concentrations further inhibited recombination and improved visible-light-driven degradation of MO and RhB [150, 151]. Sr-doped α-Bi_2O_3 nanosheets, particularly with 7.5 wt% Sr, demonstrated enhanced MB degradation, while Ce- and Nd-doped Bi_2O_3 achieved superior Acid Yellow 29 and Brilliant Blue degradation [152]. Fe-doped porous β-Bi_2O_3 microspheres with 4 mol% Fe displayed the best MO degradation due to facilitated electron–hole migration [153].

Bi_2O_3 has been successfully hybridized with carbon-based materials to further enhance photocatalytic activity. Bi_2O_3/carbon quantum dot (CQD) composites demonstrated significantly higher RhB degradation than pure Bi_2O_3 due to up-conversion properties of CQDs and enhanced charge separation [154]. Raza et al. incorporated Nb and Mn dopants into Bi_2O_3, improving MB and RhB degradation, while La/Ce co-doped Bi_2O_3 composites demonstrated synergetic suppression of electron–hole recombination and improved Acid Orange II degradation [155]. Hao et al. synthesized a C/Bi/Bi_2O_3 composite that achieved higher degradation of 2,4-dichlorophenol (2,4-DCP) owing to improved light absorption and carrier separation provided by metallic Bi and residual carbon [156]. Se-doped α-Bi_2O_3 also improved MB degradation by narrowing the band gap and suppressing recombination, while La/Er doping further enhanced Acid Yellow 29 and Acid Green 25 degradation [157].

Heterostructures of Bi_2O_3 with other semiconductors have been widely developed to optimize charge separation and extend light absorption. Bi_2O_3/TiO_2 composites synthesized by solvothermal and sol–gel methods exhibited enhanced RhB degradation due to improved surface area and heterojunction formation [159].

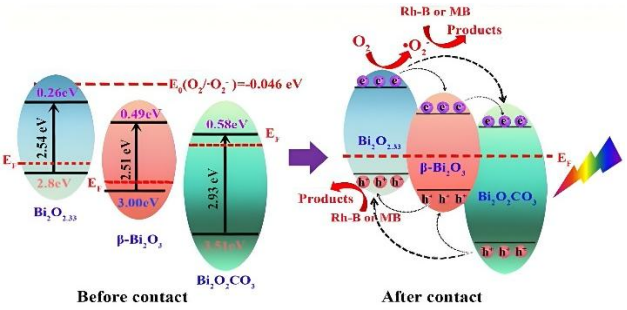

Fig. 16. Photocatalytic mechanism of 3D β-Bi_2O_3/$Bi_2O_{2.33}$@$Bi_2O_2CO_3$ under visible light [158].

Bi_2O_3/ZnO nanofibers and bentonite-supported Bi_2O_3-ZnO hybrids showed superior RhB, Acid Black 1, and Trypan Blue degradation, with optimal activity achieved at 9 wt% bentonite support (Fig. 15) [139]. Bi_2O_3-CeO_2-ZnO composites fabricated by microwave-assisted hydrothermal routes exhibited even higher performance than TiO_2-P25, highlighting synergistic effects between multiple semiconductors.

Other promising systems include Bi_2O_3/CeO_2 porous composites with improved surface area [170], Bi_2O_3/$BaTiO_3$ with 60% Bi_2O_3 composition achieving optimal RhB degradation, and Bi_2O_3/$SrFe_{12}O_{19}$ p–n heterojunctions that benefitted from magnetic field effects to enhance MB degradation [160]. CoNi/Bi_2O_3/BiOCl hybrid structures also demonstrated superior RhB removal [161]. Ternary β-Bi_2O_3/$Bi_2O_{2.33}$@$Bi_2O_2CO_3$ composites exhibited hierarchical heterostructures with enhanced charge migration, as shown in Fig. 16 [158]. Bi_2O_3/Bi_2WO_6 heterojunctions and Bi_2O_3/$FeVO_4$ composites further confirmed that heterostructures consistently outperform individual components for MO and MG degradation [174]. Finally, Bi_2O_3/g-C_3N_4 Z-scheme photocatalysts exhibited excellent phenol degradation, with the Z-scheme mechanism enabling more efficient charge transfer while preserving high redox potential[162].

Bi_2O_3, despite its intrinsic limitations, has emerged as a versatile visible-light-responsive photocatalyst. Its photocatalytic performance is significantly influenced by polymorphic phase, morphology, and nanostructure design. Doping with transition metals and rare earths enhances charge separation and band gap modulation, while hybridization with carbonaceous materials and integration into heterostructures with other semiconductors suppresses recombination and extends spectral response. Current research demonstrates that engineered Bi_2O_3 nanostructures, especially α/β heterojunctions, doped composites, and multicomponent heterostructures, hold strong promise for wastewater treatment and environmental remediation.

9. Synthesis Methods for Rare-Earth-Modified Metal Oxides

The synthesis of rare-earth-doped metal oxides is crucial for enhancing photocatalytic efficiency,

morphology, and stability. Several methods have been developed, each offering unique advantages and limitations. A comparative overview is provided in Table 2.

Table 2. Comparative Overview of Synthesis Methods

Method	Advantages	Limitations	Example	Ref.
Sol-Gel	High purity, uniform size	Time-consuming	La^{3+}-TiO_2 at 600 °C	[163]
Hydrothermal	Controlled crystal growth, high crystallinity	Requires autoclave, prolonged reaction time	Ce-ZnO at 180 °C	[164]
Solution Combustion	Fast, high surface area	Hard to control particle size	La, Sm-CeO_2 at 600 °C	[165]
Microwave-Assisted	Rapid synthesis, energy efficient	Requires precise reaction control	Eu^{3+}-TiO_2	[166]
Electrochemical Deposition	Uniform thin films, direct substrate integration	Limited to thin films, requires setup	Ce^{3+}-SnO_2 films	[167]

9.1 Sol-gel method

This bottom-up technique involves hydrolysis and condensation of metal precursors to form a gel, which is calcined into nanomaterials. For example, La^{3+}–TiO_2 was synthesized using titanium isopropoxide and $La(NO_3)_3{\cdot}6H_2O$, with hydrolysis at 60–80 °C and calcination at 500–600 °C. The method provides high-purity, uniform particles with excellent composition control, though it is time-consuming and requires multiple steps [163].

9.2 Hydrothermal Method

Hydrothermal synthesis employs high temperature and pressure in aqueous media to yield crystalline nanostructures with defined morphology. Ce-doped ZnO was prepared from $Zn(NO_3)_2{\cdot}6H_2O$ and $Ce(NO_3)_3{\cdot}6H_2O$ at 180 °C for 12 h in an autoclave, followed by drying and annealing. The technique produces highly crystalline materials with minimal defects but requires specialized equipment and long reaction durations [164].

9.3 Solution combustion method

This method relies on exothermic redox reactions between metal nitrates and organic fuels to rapidly generate nanoparticles. La, Sm–CeO_2 was synthesized using citric acid as fuel, with auto-ignition at 600 °C. It enables fast, energy-efficient synthesis of porous materials, though particle size and uniformity are difficult to control [165].

9.4 Microwave-assisted synthesis

Microwave irradiation accelerates reaction kinetics, leading to rapid and uniform nucleation. Eu^{3+}–TiO_2 was synthesized using titanium tetrachloride and europium nitrate under 500 W microwaves for 30 min, followed by calcination. The process is energy efficient and rapid but requires precise control of power and reaction time [166].

9.5 Electrochemical deposition

In this approach, metal and dopant ions are electrochemically deposited onto conductive substrates, yielding thin oxide films. For instance, Ce^{3+}–SnO_2 films were prepared using tin sulfate and cerium nitrate electrolytes at −1.2 V vs. Ag/AgCl for 15 min, then annealed at 400 °C. The method provides uniform coatings and direct integration but is restricted to thin-film synthesis [168].

Synthesis methods strongly influence the photocatalytic efficiency and scalability of rare-earth-modified oxides. While sol–gel and hydrothermal routes remain reliable for high-purity, crystalline nanostructures, faster methods such as microwave-assisted and solution combustion provide energy efficiency and high surface areas. Electrochemical deposition is particularly suited for thin-film applications. Despite progress, challenges remain in controlling particle morphology, reaction time, and scalability. Future research should explore hybrid and environmentally friendly synthesis strategies to achieve industrially viable photocatalysts for wastewater treatment and pollutant degradation.

10. Rare-Earth-Doped Metal Oxides and Nanocomposites

Rare-earth-doped metal oxides and nanocomposites are highly effective in pollutant degradation, but their environmental sustainability requires careful evaluation. A major concern is nanoparticle toxicity, as accumulation in ecosystems may disrupt aquatic cellular functions and cause bioaccumulation. Mining and processing of rare-earths are energy-intensive, generating hazardous wastes and leaching heavy metals that contaminate soil and water. Large-scale synthesis and disposal of nanocomposites also raise risks of nanoparticle release. To mitigate these issues, eco-friendly synthesis, biodegradable supports, and green chemistry strategies are being developed. Balancing environmental risks with photocatalytic benefits is essential for sustainable wastewater treatment technologies.

10.1 Metal oxides as photocatalysts

Metal oxides are crystalline materials of metal cations and oxide anions, exhibiting photoluminescence, UV absorption, dichroism, and catalytic properties. Their nanoscale dimensions provide high surface-to-volume ratios, abundant surface atoms, and unique electronic

structures that enhance reactivity compared to bulk forms. Materials such as SnO_2, TiO_2, CeO_2, ZnO, CuO, and ZrO_2 exhibit catalytic activity useful for wastewater remediation [169-172]. The performance of these nanoparticles depends strongly on size, shape, and morphology [173]. Rare-earth doping significantly enhances photocatalytic activity by modifying electronic structures, improving charge separation, and extending light absorption into the visible spectrum. Cerium (Ce) promotes oxygen vacancies through Ce^{3+}/Ce^{4+} cycling, enhancing redox activity. Europium (Eu) improves light absorption and charge storage, Lanthanum (La) increases surface area and stability, Samarium (Sm) introduces mid-gap states for visible-light photocatalysis, and Gadolinium (Gd) enhances charge transport via magnetic effects [11, 174, 175]. Collectively, these modifications increase pollutant degradation rates, stability, and visible-light performance, making RE-doped oxides suitable for next-generation photocatalysts.

Practical applications include degradation of industrial dyes such as methylene blue (MB), rhodamine B (RhB), and Rose Bengal (RB). Ce-doped TiO_2 achieved up to 95% MB degradation under visible light, while La-doped ZnO improved RhB degradation by enhancing charge separation [176, 177]. RE-modified oxides are also effective against pharmaceuticals (tetracycline, ciprofloxacin, ibuprofen) and pesticides (atrazine, chlorpyrifos, imidacloprid), demonstrating broad applicability in water remediation.

10.2 Photocatalytic activity of MO and effect of rare-earth composites

Photocatalysis begins with light absorption above the bandgap energy, generating electron–hole (e^-/h^+) pairs that drive redox reactions on the catalyst surface. Metal oxides such as TiO_2 dominate photocatalysis due to their stability, optical activity, and low cost [178]. TiO_2 exists as rutile, anatase, and brookite, with anatase showing superior activity owing to its open structure. Narrow bandgap oxides (CuO, V_2O_5, WO_3, Fe_2O_3) absorb visible light but suffer from fast e^-/h^+ recombination [179].

Rare-earth doping addresses these issues by introducing mid-gap states, oxygen vacancies, and charge-trapping sites, reducing recombination and shifting light absorption to the visible region [180]. For instance, Nd-doped SnO_2 improved phenol degradation from 24% (undoped) to 95% at 0.6 wt% Nd, while La-doped SnO_2 enabled complete phenol decomposition. Ce^{3+}-doped TiO_2 nanowire arrays degraded 90% of toluidine blue O (TBO) in 80 min, and Eu^{3+}-doped TiO_2 achieved significant RhB degradation in 120 min [181, 182]. Gd-doped TiO_2 further enhanced MB photodegradation efficiency to 90% compared to 76% for pristine TiO_2, though excessive doping reduced performance due to charge recombination [190]. Similarly, Sm-doped ZnO achieved 95.8% Congo Red removal under optimized conditions, showing doping's strong influence on efficiency (Fig. 17, Fig. 18).

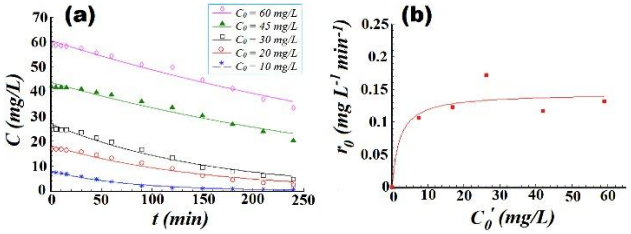

Fig. 17. (a) CR dye decay kinetics and (b) relation of r_0 with initial dye concentration using ZS (ZnO:Sm) [181].

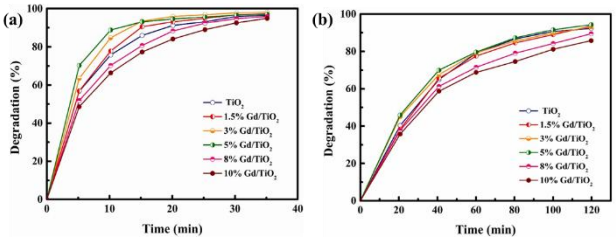

Fig. 18. MB degradation curves under (a) visible light and (b) simulated sunlight [183].

10.3 Photocatalytic activity of metal oxide

Improving photocatalytic efficiency requires enhanced light capture, charge separation, and transfer. High recombination rates and wide bandgaps limit standalone metal oxides [184]. To overcome these, composites incorporating graphene, ferrites, or transition metal oxides have been developed [185, 186].

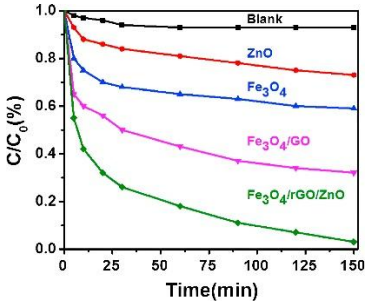

Fig. 19. Degradation of MB by photo-Fenton using different samples [187].

For example, V_2O_5 nanorods degraded only 66.85% of Victoria Blue (VB) dye under visible light, while GO–V_2O_5 composites achieved 97.95% degradation in 90 min due to improved charge transport by graphene oxide [188]. Similarly, rGO–Fe_3O_4/TiO_2 composites achieved 99% MG and 97% MB degradation, compared to 67% and 62% with TiO_2 alone (Fig. 20) [189]. A ZnO–Fe_3O_4/rGO nanocomposite removed 97% MB in 150 min under visible light, compared to 45% with Fe_3O_4/GO (Fig. 19) [187]. These examples highlight how integrating rare-earth doping with nanocomposite design markedly enhances photocatalytic efficiency.

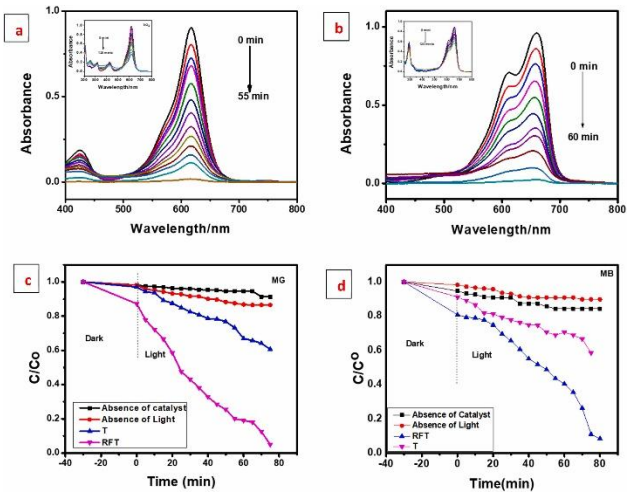

Fig. 20. Absorbance of MG (a) and MB (b), and photodegradation of MG (c) and MB (d) using TiO_2 and rGO-Fe_3O_4/TiO_2 under UV/Visible light [189].

Rare-earth-doped metal oxides and nanocomposites combine tunable electronic structures with high surface reactivity, enabling efficient degradation of dyes, pharmaceuticals, and pesticides. Challenges remain in minimizing environmental risks and optimizing synthesis for scalability. Future efforts should integrate RE-doping with composite strategies (graphene, ferrites, heterojunctions) to produce stable, visible-light-active, and eco-friendly photocatalysts for sustainable wastewater treatment.

Conclusion

The persistent release of dyes and other hazardous compounds into aquatic environments underscores the urgent need for efficient and sustainable treatment technologies. Semiconductor photocatalysis has proven to be a powerful approach for wastewater remediation, particularly due to its ability to harness solar energy and drive the mineralization of complex pollutants into non-toxic end-products. Classical oxides such as TiO_2, ZnO, WO_3, and Fe_2O_3 continue to dominate the field, yet their practical implementation is hindered by intrinsic limitations including wide band gaps, charge-carrier recombination, and photocorrosion.

Recent advances demonstrate that these challenges can be mitigated through rational materials engineering. Band-gap tuning, heterostructure construction, cocatalyst loading, and hybridization with carbonaceous supports markedly improve charge separation and visible-light utilization. Doping strategies, particularly with rare-earth elements, offer additional control over optical absorption and defect chemistry, enabling higher photocatalytic activity and stability. Comparative data from diverse synthesis techniques, such as sol–gel, hydrothermal, microwave-assisted, and combustion methods, highlight the critical role of fabrication routes in tailoring microstructure and performance.

Despite these promising developments, several barriers remain for large-scale application. Photocatalyst recovery and reusability, potential secondary environmental impacts of nanomaterials, and energy requirements under real sunlight must be carefully addressed. Furthermore, translating laboratory-scale efficiencies to continuous-flow, industrial-scale systems requires integration with reactor engineering, membrane technologies, and renewable power inputs.

Overall, the body of evidence indicates that photocatalytic water treatment has advanced from a proof-of-concept technology to a highly adaptable platform with realistic potential for deployment. Future research should emphasize multi-component systems that balance activity, stability, and cost, alongside comprehensive life-cycle assessments to ensure environmental safety. With these considerations, photocatalysis can become a cornerstone technology in achieving clean and sustainable water management.

Future Outlook

Looking ahead, the field of photocatalysis is poised to benefit from several emerging trends. Plasmonic and two-dimensional materials offer opportunities to broaden light absorption and accelerate surface reactions, while defect engineering and atomic-level doping strategies may deliver precise control over charge-carrier dynamics. The integration of artificial intelligence and high-throughput computational screening is expected to accelerate the discovery of novel photocatalysts with optimized performance-to-cost ratios. At the application level, coupling photocatalysis with membrane separation, electrocatalysis, or microbial processes could enable hybrid systems with superior efficiency and robustness. Finally, embedding life-cycle assessment and circular-economy principles into photocatalyst design will be critical to ensure that next-generation systems are not only highly effective but also environmentally responsible and scalable.

References

[1] Garg, S., et al., Impact of industrial wastewater on environment and human health, in Advanced industrial wastewater Treatment and Reclamation of water: comparative Study of water pollution Index during pre-industrial, industrial Period and Prospect of wastewater Treatment for water resource conservation. 2021, Springer. p. 197-209.

[2] Singh, S., A. Sharma, and R. Malviya, Industrial wastewater: health concern and treatment strategies. The Open Biology Journal, 2021. 9(1).

[3] Alsukaibi, A.K., Various approaches for the detoxification of toxic dyes in wastewater. Processes, 2022. 10(10): p. 1968.

[4] Xiong, L. and J. Tang, Strategies and challenges on selectivity of photocatalytic oxidation of organic substances. Advanced Energy Materials, 2021. 11(8): p. 2003216.

[5] Rani, M., et al., Recent updates on remediation approaches of environmentally occurring pollutants using visible light-active nano-photocatalysts. Environmental Science and Pollution Research, 2024. 31(15): p. 22258-22283.
[6] Bakiro, M.Y., Synthesis, Characterization, Electronic Structure of Reduced Graphene Oxide and NH_2-MIL-125 (Ti) Modified $BiNbO_4$ and Their Photocatalytic Activities. 2020.
[7] Yu, H., et al., Modulation of Bi2MoO6-based materials for photocatalytic water splitting and environmental application: a critical review. Small, 2019. 15(23): p. 1901008.
[8] Dlugosch, M., et al., Experimental investigation of hybrid material systems consisting of advanced composites and sheet metal. Composite Structures, 2016. 152: p. 840-849.
[9] Patil, A.S., et al., Synthesis techniques and applications of rare earth metal oxides semiconductors: A review. Chemical Physics Letters, 2022. 796: p. 139555.
[10] Prabhu, P., V. Jose, and J.M. Lee, Heterostructured catalysts for electrocatalytic and photocatalytic carbon dioxide reduction. Advanced Functional Materials, 2020. 30(24): p. 1910768.
[11] Zheng, B., et al., Rare-earth doping in nanostructured inorganic materials. Chemical Reviews, 2022. 122(6): p. 5519-5603.
[12] Abou El-Nour, K.M., et al., Synthesis and applications of silver nanoparticles. Arabian journal of chemistry, 2010. 3(3): p. 135-140.
[13] Adams, L.K., D.Y. Lyon, and P.J. Alvarez, Comparative eco-toxicity of nanoscale TiO2, SiO2, and ZnO water suspensions. Water research, 2006. 40(19): p. 3527-3532.
[14] Shon, H., S. Vigneswaran, and S. Snyder, Effluent organic matter (EfOM) in wastewater: constituents, effects, and treatment. Critical reviews in environmental science and technology, 2006. 36(4): p. 327-374.
[15] Kapoor, R.T., et al., Exploiting microbial biomass in treating azo dyes contaminated wastewater: Mechanism of degradation and factors affecting microbial efficiency. Journal of Water Process Engineering, 2021. 43: p. 102255.
[16] Velusamy, S., et al., A review on heavy metal ions and containing dyes removal through graphene oxide-based adsorption strategies for textile wastewater treatment. The Chemical Record, 2021. 21(7): p. 1570-1610.
[17] Solayman, H., et al., Performance evaluation of dye wastewater treatment technologies: A review. Journal of Environmental Chemical Engineering, 2023. 11(3): p. 109610.
[18] Lellis, B., et al., Effects of textile dyes on health and the environment and bioremediation potential of living organisms. Biotechnology Research and Innovation, 2019. 3(2): p. 275-290.
[19] Sivakumar, V., et al., Ultrasound assisted enhancement in natural dye extraction from beetroot for industrial applications and natural dyeing of leather. Ultrasonics Sonochemistry, 2009. 16(6): p. 782-789.
[20] Mohammadi, N., et al., Adsorption process of methyl orange dye onto mesoporous carbon material–kinetic and thermodynamic studies. Journal of colloid and interface science, 2011. 362(2): p. 457-462.
[21] Soares, G.M., M.P. de Amorim, and M. Costa-Ferreira, Use of laccase together with redox mediators to decolourize Remazol Brilliant Blue R. Journal of Biotechnology, 2001. 89(2-3): p. 123-129.
[22] Hanafi, M.F. and N. Sapawe, A review on the water problem associate with organic pollutants derived from phenol, methyl orange, and remazol brilliant blue dyes. Materials Today: Proceedings, 2020. 31: p. A141-A150.
[23] Al-Gheethi, A.A., et al., Sustainable approaches for removing Rhodamine B dye using agricultural waste adsorbents: A review. Chemosphere, 2022. 287: p. 132080.
[24] Thevarajah, S., T.L. Huston, and R.M. Simmons, A comparison of the adverse reactions associated with isosulfan blue versus methylene blue dye in sentinel lymph node biopsy for breast cancer. The American journal of surgery, 2005. 189(2): p. 236-239.
[25] Chen, X., J. Li, and F. Chen, Photocatalytic degradation of MB by novel and environmental ZnO/Bi2WO6-CC hierarchical heterostructures. Materials Characterization, 2022. 189: p. 111961.
[26] Demartis, S., et al., Nanotechnology-based rose Bengal: A broad-spectrum biomedical tool. Dyes and Pigments, 2021. 188: p. 109236.
[27] Ahmad, M.A., et al., Sorption studies of methyl red dye removal using lemon grass (Cymbopogon citratus). Chemical Data Collections, 2019. 22: p. 100249.
[28] Ben Mansour, H., et al., Acid violet 7 and its biodegradation products induce chromosome aberrations, lipid peroxidation, and cholinesterase inhibition in mouse bone marrow. Environmental Science and Pollution Research, 2010. 17(7): p. 1371-1378.
[29] Wang, X., et al., Degradation of reactive brilliant red in aqueous solution by ultrasonic cavitation. Ultrasonics Sonochemistry, 2008. 15(1): p. 43-48.
[30] Hernández-Zamora, M. and F. Martínez-Jerónimo, Exposure to the azo dye Direct blue 15 produces toxic effects on microalgae, cladocerans, and zebrafish embryos. Ecotoxicology, 2019. 28(8): p. 890-902.
[31] Ikram, M., et al., A review of photocatalytic characterization, and environmental cleaning, of metal oxide nanostructured materials. Sustainable Materials and Technologies, 2021. 30: p. e00343.
[32] Ikram, M., et al., Dye degradation performance, bactericidal behavior and molecular docking analysis of Cu-doped TiO 2 nanoparticles. RSC advances, 2020. 10(41): p. 24215-24233.
[33] Ikram, M., et al., 2D chemically exfoliated hexagonal boron nitride (hBN) nanosheets doped with Ni: synthesis, properties and catalytic application for the treatment of industrial wastewater. Applied Nanoscience, 2020. 10(9): p. 3525-3528.
[34] Raza, A., et al., A comparative study of dirac 2D materials, TMDCs and 2D insulators with regard to their structures and photocatalytic/sonophotocatalytic behavior. Applied Nanoscience, 2020. 10(10): p. 3875-3899.
[35] Malathi, A. and J. Madhavan, A review on BiVO4 photocatalyst: activity enhancement methods for solar photocatalytic applications. Applied Catalysis A: General, 2018. 555: p. 47-74.
[36] Imanishi, A. and K.-i. Fukui, Atomic-scale surface local structure of TiO2 and its influence on the water photooxidation process. The Journal of Physical Chemistry Letters, 2014. 5(12): p. 2108-2117.
[37] Zhang, H., et al., Hydrogen-bond bridged water oxidation on {001} surfaces of anatase TiO2. The Journal of Physical Chemistry C, 2017. 121(4): p. 2251-2257.
[38] Sakai, N., et al., Enhancement of the photoinduced hydrophilic conversion rate of TiO2 film electrode

surfaces by anodic polarization. The Journal of Physical Chemistry B, 2001. 105(15): p. 3023-3026.
[39] Shirasawa, T., et al., Structural change of the rutile–TiO2 (110) surface during the photoinduced wettability conversion. The Journal of Physical Chemistry C, 2016. 120(51): p. 29107-29115.
[40] Sun, R.-D., et al., Photoinduced surface wettability conversion of ZnO and TiO2 thin films. The Journal of Physical Chemistry B, 2001. 105(10): p. 1984-1990.
[41] Cummings, C.Y., et al., New insights into water splitting at mesoporous α-Fe2O3 films: a study by modulated transmittance and impedance spectroscopies. Journal of the American Chemical Society, 2012. 134(2): p. 1228-1234.
[42] Zhang, Y., et al., Pivotal role and regulation of proton transfer in water oxidation on hematite photoanodes. Journal of the American Chemical Society, 2016. 138(8): p. 2705-2711.
[43] Montoya, J.F., et al., Comprehensive kinetic and mechanistic analysis of TiO2 photocatalytic reactions according to the direct–indirect model:(II) Experimental validation. The Journal of Physical Chemistry C, 2014. 118(26): p. 14276-14290.
[44] Chang, X., T. Wang, and J. Gong, CO 2 photo-reduction: insights into CO 2 activation and reaction on surfaces of photocatalysts. Energy & Environmental Science, 2016. 9(7): p. 2177-2196.
[45] Zhu, S. and D. Wang, Photocatalysis: basic principles, diverse forms of implementations and emerging scientific opportunities. Advanced Energy Materials, 2017. 7(23): p. 1700841.
[46] Gattrell, M., N. Gupta, and A. Co, A review of the aqueous electrochemical reduction of CO2 to hydrocarbons at copper. Journal of electroanalytical Chemistry, 2006. 594(1): p. 1-19.
[47] Lee, J., D.C. Sorescu, and X. Deng, Electron-induced dissociation of CO2 on TiO2 (110). Journal of the American Chemical Society, 2011. 133(26): p. 10066-10069.
[48] Liu, Y., et al., Chemical adsorption enhanced CO2 capture and photoreduction over a copper porphyrin based metal organic framework. ACS applied materials & interfaces, 2013. 5(15): p. 7654-7658.
[49] Guo, Q., et al., Stepwise photocatalytic dissociation of methanol and water on TiO2 (110). Journal of the American Chemical Society, 2012. 134(32): p. 13366-13373.
[50] Liu, R., et al., Water splitting by tungsten oxide prepared by atomic layer deposition and decorated with an oxygen-evolving catalyst. Angew. Chem. Int. Ed, 2011. 50(2): p. 499-502.
[51] Mi, Q., et al., Photoelectrochemical oxidation of anions by WO 3 in aqueous and nonaqueous electrolytes. Energy & Environmental Science, 2013. 6(9): p. 2646-2653.
[52] Fang, L.J., et al., Facile fabrication of large-aspect-ratio g-C3N4 nanosheets for enhanced photocatalytic hydrogen evolution. ACS Sustainable Chemistry & Engineering, 2017. 5(3): p. 2039-2043.
[53] Liu, J., et al., Metal-free efficient photocatalyst for stable visible water splitting via a two-electron pathway. Science, 2015. 347(6225): p. 970-974.
[54] Li, X., et al., Engineering heterogeneous semiconductors for solar water splitting. Journal of Materials Chemistry A, 2015. 3(6): p. 2485-2534.
[55] Moniz, S.J., J. Zhu, and J. Tang, 1D Co-Pi modified BiVO4/ZnO junction cascade for efficient photoelectrochemical water cleavage. Advanced Energy Materials, 2014. 4(10): p. 1301590.
[56] Ibhadon, A.O. and P. Fitzpatrick, Heterogeneous photocatalysis: recent advances and applications. Catalysts, 2013. 3(1): p. 189-218.
[57] Rueda-Marquez, J.J., et al., A critical review on application of photocatalysis for toxicity reduction of real wastewaters. Journal of Cleaner Production, 2020. 258: p. 120694.
[58] Chen, X., et al., Preparation of ZnO photocatalyst for the efficient and rapid photocatalytic degradation of azo dyes. Nanoscale research letters, 2017. 12(1): p. 143.
[59] Gu, C., et al., A promising carbon fiber-based photocatalyst with hierarchical structure for dye degradation. RSC Advances, 2017. 7(36): p. 22234-22242.
[60] Nekouei, S., F. Nekouei, and H. Kargarzadeh, Synthesis of ZnO photocatalyst modified with activated carbon for a perfect degradation of ciprofloxacin and its secondary pollutants. Applied Organometallic Chemistry, 2018. 32(3): p. e4198.
[61] Atchudan, R., et al., Biowaste-derived heteroatom-doped porous carbon as a sustainable electrocatalyst for hydrogen evolution reaction. Catalysts, 2023. 13(3): p. 542.
[62] Hassan, S.S., et al., Green synthesis and characterization of ZnO nanoparticles for photocatalytic degradation of anthracene. Advances in Natural Sciences: Nanoscience and Nanotechnology, 2015. 6(4): p. 045012.
[63] Bae, K.-L., et al., Colloidal zinc oxide-copper (I) oxide nanocatalysts for selective aqueous photocatalytic carbon dioxide conversion into methane. Nature communications, 2017. 8(1): p. 1156.
[64] Türkyılmaz, Ş.Ş., N. Güy, and M. Özacar, Photocatalytic efficiencies of Ni, Mn, Fe and Ag doped ZnO nanostructures synthesized by hydrothermal method: The synergistic/antagonistic effect between ZnO and metals. Journal of Photochemistry and Photobiology A: Chemistry, 2017. 341: p. 39-50.
[65] Chaudhary, D., et al., ZnO nanoparticles decorated multi-walled carbon nanotubes for enhanced photocatalytic and photoelectrochemical water splitting. Journal of Photochemistry and Photobiology A: Chemistry, 2018. 351: p. 154-161.
[66] Chang, Y.-C., et al., Construction of CuO/In 2 S 3/ZnO heterostructure arrays for enhanced photocatalytic efficiency. Nanoscale, 2017. 9(35): p. 13235-13244.
[67] Zhang, Y., et al., Piezotronic-effect-enhanced Ag 2 S/ZnO photocatalyst for organic dye degradation. RSC Advances, 2017. 7(76): p. 48176-48183.
[68] Wang, F., et al., Enhanced photocatalytic properties of ZnO nanorods by electrostatic self-assembly with reduced graphene oxide. Physical Chemistry Chemical Physics, 2018. 20(10): p. 6959-6969.
[69] Wang, G., et al., ZnO/MoX 2 (X= S, Se) composites used for visible light photocatalysis. Rsc Advances, 2018. 8(20): p. 10828-10835.
[70] Naseri, A., et al., Tuning composition of electrospun ZnO/CuO nanofibers: toward controllable and efficient solar photocatalytic degradation of organic pollutants. The Journal of Physical Chemistry C, 2017. 121(6): p. 3327-3338.
[71] Lu, L., et al., One-step in situ growth of ZnS nanoparticles on reduced graphene oxides and their improved lithium storage performance using sodium carboxymethyl cellulose binder. RSC advances, 2018. 8(17): p. 9125-9133.

[72] Donat, F., et al., ZnO nanoparticles sensitized by CuInZnxS2+ x quantum dots as highly efficient solar light driven photocatalysts. Beilstein journal of nanotechnology, 2017. 8(1): p. 1080-1093.
[73] Razavi-Khosroshahi, H., et al., High-pressure zinc oxide phase as visible-light-active photocatalyst with narrow band gap. Journal of Materials Chemistry A, 2017. 5(38): p. 20298-20303.
[74] Hong, D., et al., High piezo-photocatalytic efficiency of CuS/ZnO nanowires using both solar and mechanical energy for degrading organic dye. ACS applied materials & interfaces, 2016. 8(33): p. 21302-21314.
[75] Thangavel, S., et al., Graphdiyne–ZnO nanohybrids as an advanced photocatalytic material. The Journal of Physical Chemistry C, 2015. 119(38): p. 22057-22065.
[76] Chanu, I., P. Krishnamurthi, and P.T. Manoharan, Effect of silver on plasmonic, photocatalytic, and cytotoxicity of gold in AuAgZnO nanocomposites. The Journal of Physical Chemistry C, 2017. 121(16): p. 9077-9088.
[77] Ma, D., et al., Highly efficient photocatalyst based on a CdS quantum dots/ZnO nanosheets 0D/2D heterojunction for hydrogen evolution from water splitting. ACS applied materials & interfaces, 2017. 9(30): p. 25377-25386.
[78] Bak, D. and J.H. Kim, Oxidation driven ZnS Core-ZnO shell photocatalysts under controlled oxygen atmosphere for improved photocatalytic solar water splitting. Journal of Power Sources, 2018. 389: p. 70-76.
[79] Cheng, Z., S. Zhao, and L. Han, A novel preparation method for ZnO/γ-Al 2 O 3 nanofibers with enhanced absorbability and improved photocatalytic water-treatment performance by Ag nanoparticles. Nanoscale, 2018. 10(15): p. 6892-6899.
[80] Alam, U., et al., Comparative photocatalytic activity of sol–gel derived rare earth metal (La, Nd, Sm and Dy)-doped ZnO photocatalysts for degradation of dyes. RSC advances, 2018. 8(31): p. 17582-17594.
[81] Bao, Y., et al., One-step hydrothermal synthesis of hollow ZnO microspheres with enhanced performance for polyacrylate. Progress in Organic Coatings, 2017. 112: p. 270-277.
[82] Ullah, R. and J. Dutta, Photocatalytic degradation of organic dyes with manganese-doped ZnO nanoparticles. Journal of Hazardous materials, 2008. 156(1-3): p. 194-200.
[83] Lei, Y., J. Huo, and H. Liao, Microstructure and photocatalytic properties of polyimide/heterostructured NiO–Fe 2 O 3–ZnO nanocomposite films via an ion-exchange technique. RSC advances, 2017. 7(64): p. 40621-40631.
[84] Pei, C., et al., Superior adsorption performance for triphenylmethane dyes on 3D architectures assembled by ZnO nanosheets as thin as~ 1.5 nm. Journal of Hazardous Materials, 2016. 318: p. 732-741.
[85] Isimjan, T.T., et al., Comprehensive study of all-solid-state Z-scheme photocatalytic systems of ZnO/Pt/CdZnS. ACS omega, 2017. 2(8): p. 4828-4837.
[86] Dong, P., et al., WO 3-based photocatalysts: morphology control, activity enhancement and multifunctional applications. Environmental Science: Nano, 2017. 4(3): p. 539-557.
[87] Katsumata, K.-i., et al., Preparation of graphitic carbon nitride (g-C3N4)/WO3 composites and enhanced visible-light-driven photodegradation of acetaldehyde gas. Journal of hazardous materials, 2013. 260: p. 475-482.
[88] Cao, L., et al., Photocatalytic energy storage ability of TiO2-WO3 composite prepared by wet-chemical technique. Journal of Environmental Sciences, 2010. 22(3): p. 454-459.
[89] Hunge, Y., et al., Degradation of organic dyes using spray deposited nanocrystalline stratified WO3/TiO2 photoelectrodes under sunlight illumination. Optical Materials, 2018. 76: p. 260-270.
[90] Wang, H., et al., Design and facile one-step synthesis of FeWO4/Fe2O3 di-modified WO3 with super high photocatalytic activity toward degradation of quasi-phenothiazine dyes. Applied Catalysis B: Environmental, 2018. 221: p. 169-178.
[91] Yao, S., et al., Hierarchical WO3 nanostructures assembled by nanosheets and their applications in wastewater purification. Journal of Alloys and Compounds, 2016. 689: p. 570-574.
[92] Yao, S., et al., Facile hydrothermal synthesis of WO3 nanorods for photocatalysts and supercapacitors. Journal of Alloys and Compounds, 2017. 724: p. 695-702.
[93] Momeni, M.M. and Y. Ghayeb, Fabrication, characterization and photocatalytic properties of Au/TiO2-WO3 nanotubular composite synthesized by photo-assisted deposition and electrochemical anodizing methods. Journal of Molecular Catalysis A: Chemical, 2016. 417: p. 107-115.
[94] Wang, Z., et al., Facile synthesis of hierarchical double-shell WO3 microspheres with enhanced photocatalytic activity. Applied Surface Science, 2017. 396: p. 492-496.
[95] Yu, J. and L. Qi, Template-free fabrication of hierarchically flower-like tungsten trioxide assemblies with enhanced visible-light-driven photocatalytic activity. Journal of Hazardous materials, 2009. 169(1-3): p. 221-227.
[96] Adhikari, S., et al., Understanding the morphological effects of WO3 photocatalysts for the degradation of organic pollutants. Advanced Powder Technology, 2018. 29(7): p. 1591-1600.
[97] Guo, X., et al., Morphology-controlled synthesis of WO 2.72 nanostructures and their photocatalytic properties. RSC advances, 2016. 6(54): p. 48537-48542.
[98] Mehmood, F., et al., Ni doped WO3 nanoplates: an excellent photocatalyst and novel nanomaterial for enhanced anticancer activities. Journal of Alloys and Compounds, 2018. 746: p. 729-738.
[99] Pirzada, B.M., et al., Efficient visible-light-driven Photocatalytic activity and enhanced charge transfer properties over Mo-doped WO3/TiO2 nanocomposites. Journal of Environmental Chemical Engineering, 2018. 6(2): p. 3204-3212.
[100] Zhang, J., et al., Facile synthesis 3D flower-like Ag@ WO3 nanostructures and applications in solar-light photocatalysis. Journal of Alloys and Compounds, 2018. 757: p. 134-141.
[101] Mehmood, F., et al., Structural, Raman and photoluminescence properties of Fe doped WO3 nanoplates with anti cancer and visible light driven photocatalytic activities. Journal of Alloys and Compounds, 2017. 728: p. 1329-1337.
[102] Ma, G., et al., Synergistic effect of Cu-ion and WO3 nanofibers on the enhanced photocatalytic degradation of Rhodamine B and aniline solution. Applied Surface Science, 2018. 451: p. 306-314.
[103] Jeevitha, G., et al., Tungsten oxide-graphene oxide (WO3-GO) nanocomposite as an efficient photocatalyst, antibacterial and anticancer agent. Journal of Physics and Chemistry of Solids, 2018. 116: p. 137-147.

[104] Ahmed, B., et al., Well-controlled in-situ growth of 2D WO3 rectangular sheets on reduced graphene oxide with strong photocatalytic and antibacterial properties. Journal of hazardous materials, 2018. 347: p. 266-278.
[105] Zhou, M., J. Yan, and P. Cui, Synthesis and enhanced photocatalytic performance of WO3 nanorods@ graphene nanocomposites. Materials Letters, 2012. 89: p. 258-261.
[106] An, X., et al., WO 3 nanorods/graphene nanocomposites for high-efficiency visible-light-driven photocatalysis and NO 2 gas sensing. Journal of Materials Chemistry, 2012. 22(17): p. 8525-8531.
[107] Gan, L., et al., Visible light induced methylene blue dye degradation photo-catalyzed by WO3/graphene nanocomposites and the mechanism. Ceramics International, 2016. 42(14): p. 15235-15241.
[108] Taha, A.A. and F. Li, Porous WO 3–carbon nanofibers: high-performance and recyclable visible light photocatalysis. Catalysis Science & Technology, 2014. 4(10): p. 3601-3605.
[109] Farhadian, M., P. Sangpour, and G. Hosseinzadeh, Preparation and photocatalytic activity of WO 3–MWCNT nanocomposite for degradation of naphthalene under visible light irradiation. Rsc Advances, 2016. 6(45): p. 39063-39073.
[110] Song, B., et al., Two-step hydrothermally synthesized carbon nanodots/WO 3 photocatalysts with enhanced photocatalytic performance. Dalton Transactions, 2017. 46(45): p. 15769-15777.
[111] Ismail, A.A., M. Faisal, and A. Al-Haddad, Mesoporous WO3-graphene photocatalyst for photocatalytic degradation of Methylene Blue dye under visible light illumination. Journal of Environmental Sciences, 2018. 66: p. 328-337.
[112] Mishra, M. and D.-M. Chun, α-Fe2O3 as a photocatalytic material: A review. Applied Catalysis A: General, 2015. 498: p. 126-141.
[113] Sundaramurthy, J., et al., Superior photocatalytic behaviour of novel 1D nanobraid and nanoporous α-Fe 2 O 3 structures. RSC Advances, 2012. 2(21): p. 8201-8208.
[114] Hosseinian, A., H. Rezaei, and A.R. Mahjoub, Preparation of nanosized iron oxide and their photocatalytic properties for congo red. World Acedemy Sci Eng Technol, 2011. 52: p. 736-739.
[115] Aprile, C., A. Corma, and H. Garcia, Enhancement of the photocatalytic activity of TiO 2 through spatial structuring and particle size control: from subnanometric to submillimetric length scale. Physical Chemistry Chemical Physics, 2008. 10(6): p. 769-783.
[116] Pradhan, G.K., S. Martha, and K. Parida, Synthesis of multifunctional nanostructured zinc–iron mixed oxide photocatalyst by a simple solution-combustion technique. ACS Applied Materials & Interfaces, 2012. 4(2): p. 707-713.
[117] Apte, S., et al., Synthesis of nanosize-necked structure α-and γ-Fe2O3 and its photocatalytic activity. Journal of the American Ceramic Society, 2007. 90(2): p. 412-414.
[118] Zhou, W., et al., Biosynthesis of mesoporous organic–inorganic hybrid Fe2O3 with high photocatalytic activity. Materials Science and Engineering: C, 2009. 29(6): p. 1893-1896.
[119] Dang, S., et al., Dark-degradation of reactive brilliant blue X-BR in aqueous solution using α-Fe2O3. Journal of non-crystalline solids, 2008. 354(45-46): p. 5018-5021.
[120] Soni, H., et al., Photo catalytic efficiency and kinetic studies of ZnO nanoparticles for the removal of basic dye Rhodamine B. Desalination and Water Treatment, 2016. 57(42): p. 19857-19864.
[121] Liu, Y., et al., Fast degradation of methylene blue with electrospun hierarchical α-Fe2O3 nanostructured fibers. Journal of sol-gel science and technology, 2011. 58(3): p. 716-723.
[122] Araujo, R., et al., α-Fe2O3 fibers: An efficient photocatalyst for dye degradation under visible light. Journal of Alloys and Compounds, 2021. 882: p. 160683.
[123] Liu, G., et al., Micro/nanostructured α-Fe 2 O 3 spheres: synthesis, characterization, and structurally enhanced visible-light photocatalytic activity. Journal of Materials Chemistry, 2012. 22(19): p. 9704-9713.
[124] Li, X., et al., Controllable fabrication, growth mechanisms, and photocatalytic properties of hematite hollow spindles. The Journal of Physical Chemistry C, 2009. 113(7): p. 2837-2845.
[125] Wang, L., et al., Electrospun hollow cage-like α-Fe 2 O 3 microspheres: synthesis, formation mechanism, and morphology-preserved conversion to Fe nanostructures. CrystEngComm, 2014. 16(46): p. 10618-10623.
[126] Huang, S., et al., Enhancing reactive oxygen species generation and photocatalytic performance via adding oxygen reduction reaction catalysts into the photocatalysts. Applied Catalysis B: Environmental, 2017. 218: p. 174-185.
[127] Ren, L., et al., Defects-engineering of magnetic γ-Fe2O3 ultrathin nanosheets/mesoporous black TiO2 hollow sphere heterojunctions for efficient charge separation and the solar-driven photocatalytic mechanism of tetracycline degradation. Applied Catalysis B: Environmental, 2019. 240: p. 319-328.
[128] Ahmmad, B., et al., Green synthesis of mesoporous hematite (α-Fe2O3) nanoparticles and their photocatalytic activity. Advanced Powder Technology, 2013. 24(1): p. 160-167.
[129] Zhang, H., et al., Fe 2 O 3/carbon quantum dots complex photocatalysts and their enhanced photocatalytic activity under visible light. Dalton Transactions, 2011. 40(41): p. 10822-10825.
[130] Aragón, F.F., et al., Effect of the thickness reduction on the structural, surface and magnetic properties of α-Fe2O3 thin films. Thin Solid Films, 2016. 607: p. 50-54.
[131] Kusior, A., et al., Shaped Fe2O3 nanoparticles–synthesis and enhanced photocatalytic degradation towards RhB. Applied surface science, 2019. 476: p. 342-352.
[132] Iandolo, B., et al., The rise of hematite: origin and strategies to reduce the high onset potential for the oxygen evolution reaction. Journal of Materials Chemistry A, 2015. 3(33): p. 16896-16912.
[133] Zeng, L., et al., The development of anticancer ruthenium (II) complexes: from single molecule compounds to nanomaterials. Chemical Society Reviews, 2017. 46(19): p. 5771-5804.
[134] Cheng, H., et al., Synergistic effect of crystal and electronic structures on the visible-light-driven photocatalytic performances of Bi 2 O 3 polymorphs. Physical Chemistry Chemical Physics, 2010. 12(47): p. 15468-15475.
[135] Xiao, X., et al., l-Asparagine-assisted synthesis of flower-like β-Bi 2 O 3 and its photocatalytic performance for the degradation of 4-phenylphenol under visible-light irradiation. RSC Advances, 2015. 5(91): p. 74977-74985.
[136] Hou, J., et al., In situ synthesis of α–β phase heterojunction on Bi2O3 nanowires with exceptional

visible-light photocatalytic performance. Applied Catalysis B: Environmental, 2013. 142: p. 504-511.
[137] Bera, K.K., et al., Synthesis of α-β Bi2O3 heterojunction photocatalyst and evaluation of reaction mechanism for degradation of RhB dye under natural sunlight. Ceramics International, 2020. 46(6): p. 7667-7680.
[138] Sonkusare, V.N., et al., Microwave-mediated synthesis, photocatalytic degradation and antibacterial activity of α-Bi2O3 microflowers/novel γ-Bi2O3 microspindles. Nano-Structures & Nano-Objects, 2018. 13: p. 121-131.
[139] Balachandran, S. and M. Swaminathan, Facile fabrication of heterostructured Bi2O3–ZnO photocatalyst and its enhanced photocatalytic activity. The Journal of Physical Chemistry C, 2012. 116(50): p. 26306-26312.
[140] Wu, Y.-C., et al., Morphology-controllable Bi2O3 crystals through an aqueous precipitation method and their photocatalytic performance. Dyes and Pigments, 2013. 98(1): p. 25-30.
[141] Liu, H., et al., Bi2O3/Bi nanocomposites confined by N-doped honeycomb-like porous carbon for high-rate and long-life lithium storage. Applied Materials Today, 2021. 22: p. 100885.
[142] Wang, J., et al., Precursor-induced fabrication of β-Bi 2 O 3 microspheres and their performance as visible-light-driven photocatalysts. Journal of Materials Chemistry A, 2013. 1(32): p. 9069-9074.
[143] Lu, Y., et al., Photoactive β-Bi2O3 architectures prepared by a simple solution crystallization method. Ceramics International, 2014. 40(9): p. 15057-15063.
[144] Niu, X., et al., Hydrothermal synthesis of Mo-C co-doped TiO2 and coupled with fluorine-doped tin oxide (FTO) for high-efficiency photodegradation of methylene blue and tetracycline: Effect of donor-acceptor passivated co-doping. Applied Surface Science, 2019. 466: p. 882-892.
[145] Bao, Y., et al., Acetic acid-assisted fabrication of hierarchical flower-like Bi2O3 for photocatalytic degradation of sulfamethoxazole and rhodamine B under solar irradiation. Journal of colloid and interface science, 2017. 505: p. 489-499.
[146] Pei, L. and N. Zhao, Facile Room-Temperature Synthesis of Z-Scheme Typed A-Bi2o3/A-Bi2o3 Homojunction Displaying High Photocatalytic Reduction of Heavy Metal Cr (Vi).
[147] Zhu, G., W. Que, and J. Zhang, Synthesis and photocatalytic performance of Ag-loaded β-Bi2O3 microspheres under visible light irradiation. Journal of alloys and compounds, 2011. 509(39): p. 9479-9486.
[148] Liu, X., et al., Enhanced photocatalytic activity of Bi2O3–Ag2O hybrid photocatalysts. Applied Surface Science, 2015. 347: p. 269-274.
[149] zhang Li, J., et al., Improved photocatalytic activity of dysprosium-doped Bi2O3 prepared by sol–gel method. Materials science in semiconductor processing, 2013. 16(2): p. 379-384.
[150] Liu, X. and Y. Kang, Synthesis and high visible-light activity of novel Bi2O3/FeVO4 heterojunction photocatalyst. Materials Letters, 2016. 164: p. 229-231.
[151] Faisal, M., et al., Hydrothermal synthesis of Sr-doped α-Bi2O3 nanosheets as highly efficient photocatalysts under visible light. Journal of Molecular Catalysis A: Chemical, 2014. 387: p. 69-75.
[152] Que, Q., et al., Bi2O3/Carbon quantum dots heterostructured photocatalysts with enhanced photocatalytic activity. Materials Letters, 2017. 209: p. 220-223.
[153] Raza, W., et al., Facile fabrication of visible light induced Bi2O3 nanorod using conventional heat treatment method. Journal of Molecular Structure, 2016. 1107: p. 39-46.
[154] Hao, Q., et al., One-pot synthesis of C/Bi/Bi2O3 composite with enhanced photocatalytic activity. Applied Catalysis B: Environmental, 2017. 219: p. 63-72.
[155] Raza, W., D. Bahnemann, and M. Muneer, A green approach for degradation of organic pollutants using rare earth metal doped bismuth oxide. Catalysis Today, 2018. 300: p. 89-98.
[156] Bian, Y., et al., Self-integrated β-Bi2O3/Bi2O2. 33@ Bi2O2CO3 ternary composites: format